EUROPEAN ORGANISATION FOR NUCLEAR RESEARCH

CERN/LHCC 2000-010
06 January 2000

# RD39 STATUS REPORT

## RD39 Collaboration

K. Borer, S. Janos and K. Pretzl
*Laboratorium für Hochenergiephysik der Universität Bern, Sidlerstarsse 5, CH-3012 Bern, Switzerland*

B. Dezillie and Z. Li
*Brookhaven National Laboratory, Upton, NY 11973-5000, USA*

C. da Viá, V. Granata, S. Watts
*Brunel University, Uxbridge, Middlesex UB8 3PH, UK*

L. Casagrande, P. Collins, S. Grohmann, E. Heijne, C. Lourenço, T.O. Niinikoski*, V.G. Palmieri* and P. Sonderegger
*CERN, CH-1211 Geneva, Switzerland*

E. Borchi, M. Bruzzi and S. Pirollo
*Dipartimento di Energetica, Universitá di Firenze, I-50139 Firenze, Italy*

S. Chapuy, Z. Dimcovski and E. Grigoriev
*Department de Radiologie, Universite de Geneve, CH-1211 Geneva, Switzerland*

W. Bell, S.R.H. Devine, V. O'Shea, G. Ruggiero and K. Smith
*Department of Physics and Astronomy, University of Glasgow, Glasgow G12 8QQ, UK*

P. Berglund
*Low Temperature Laboratory, Helsinki University of Technology, FI-02150 Espoo, Finland*

W. de Boer, F. Hauler, S. Heising and L. Jungermann
*IEKP University of Karlsruhe, D-76128 Karlsruhe, Germany*

M. Abreu, P. Rato Mendes and P. Sousa
*LIP, Av. E. Garcia, P-1000 Lisbon, Portugal*

V. Cindro, M. Mikuz and M. Zavrtanik
*Jozef Stefan Institute, Exp. Particle Physics Dep., PO Box 3000, 1001 Ljubljana, Slovenia*

A. Esposito, I. Konorov and S. Paul
*Physik Department E18, Technische Universität München, D-85748 Garching, Germany*

S. Buontempo, N. D'Ambrosio and S. Pagano
*Dipartimento di Fisica, Universitá "Federico II" and INFN, I-80125 Napoli, Italy*

V. Eremin and E. Verbitskaya
*Ioffe Physico-Technical Institute, Russian Academy of Sciences, St. Petersburg 194021, Russia*



* co-spokesperson

# 1 INTRODUCTION

In the Addendum to the RD39 proposal [1], approved on 23 October 1998 by the LHCC, we proposed to study cryogenic silicon detectors in view of their use in applications requiring extreme radiation hardness. Our main goal, in addition to deepening the understanding of the physics of various sensor types, was to demonstrate operation with *in situ* irradiation at low temperatures. We also proposed to demonstrate the use of on-detector CMOS readout electronics at low temperatures, and to show that simple and economic means are available for the cooling of the detectors and electronics at the required operating temperature. We shall report here the successful achievement of these goals. It is now clear that operation at cryogenic temperature thus leads to unprecedented radiation hardness for standard silicon detectors.

The Lazarus effect, which we also further investigated, is phenomenologically described as the recovery of the Charge Collection Efficiency (CCE) of heavily irradiated silicon detectors when cooled to cryogenic temperatures. This was observed for the first time in 1998 [2] and the results of RD39 have been already published [3] on the studies of the CCE, extended up to fluences about one order of magnitude higher than the limit of survival for usual silicon detectors. Results on the CCE and track resolution for a proton irradiated double-sided microstrip detector have been also already published [4].

In this RD39 Status Report we shall review all our experimental work carried out during the period from October 1998 through the end of 1999. In addition to a summary of the published work quoted above, we include here the preliminary results on $p^+/n/p^+$ diodes, on segmented devices, and on *in-situ* irradiated devices. The annealing effects were also investigated on some devices and are summarized here. The design and construction of a prototype heavy ion beam hodoscope detector, named "Beamscope" is described and preliminary test results are shown. Moreover, we shall describe the design, construction and tests of several cooling systems developed for laboratory and beam tests.

This Report is organized in the following way. In Section 2 we shall describe the processing and irradiation procedures of the devices which were investigated. The experimental studies of the Lazarus effect using simple diode and symmetric structures are summarized in Section 3, and the results on the microstrip detectors are reported in Section 4. In Section 5 we shall discuss the design and construction of the cooling systems used for obtaining the preliminary results reported here, and describe also the conceptual design work for closed-cycle refrigerators, which can be used in high-radiation areas. After giving in Section 6 our

conclusions and the summary of implications for the LHC experiments, we shall outline our future program in Section 7.

## 2 PROCESSING AND IRRADIATION OF THE SILICON DETECTORS

### 2.1 Diode and pad detectors

Various prototype Si detectors were processed at Brookhaven National Laboratory (BNL). In all cases, simple processing technology involving at most three mask steps was used. The goal was to qualify a reliable and cheap detector technology that could take full advantage of the operation at low temperatures. All these structures have a single guard-ring. A set of three masks was designed for processing on 4-inch wafers of different thickness and resistivity. This mask includes several types of segmentation: single-pad and multipad diodes, and microstrip detectors with various pitches and strip widths. The processed structures are described below.

#### *2.1.1 Al/p$^+$/n/n$^+$/Al or Al/p$^+$/n/p$^+$/Al pad and strip detectors*

This is the process with which the detectors discussed in Sections 3 and 4 were produced, with the exception of the sensors of the DELPHI module. A 0.47 μm $SiO_2$ layer was thermally grown on 4" n-type Si wafers. The first mask, called P-implant, was used to open up windows (with 0.1 μm $SiO_2$ remaining) in the front side that define the detector geometry and allow B ion implant to go through to form $p^+$ layer. During the etching of $SiO_2$ windows on the front side, the back $SiO_2$ was etched uniformly, which allows a uniform implantation of P or B ions for the $n^+$ and $p^+$ back layers respectively. The wafers were then ion implanted on the front side (B ions) and on the backside (P ions or B ions). After a thermal activation anneal in $N_2$, another mask called Step-cut was used to cut the remaining 0.1 μm $SiO_2$ down to the bare Si on the front side, while the $SiO_2$ layer on the back side was cut entirely. Al layers of 0.25 μm thickness were then sputtered on both sides. The third and final mask called Al-cover was then used to define the metal contacts on the front side. After a final thermal sintering in the forming gas ($N_2$ with 4% $H_2$), the detectors were ready for testing.

#### *2.1.2 Al/n$^+$/n/n$^+$/Al resistor-type pad detectors*

The processing technology is similar to that used in above except: a) the first $SiO_2$ cut was down to bare Si, thus eliminating the Step-cut mask step; and b) P ions were used for implants on both sides. In this case, the processing is even simpler: only two mask steps were used. This process is currently under investigation.

### *2.1.3 Al/lapped n-Si/Al resistor-type pad detectors*

This is the detector configuration with simplest processing technology. After the lapping of n-type Si wafers on both sides, Al layers were sputtered on both sides of the wafer. Only one mask named Al-cover was used to define Al contact patterns on one side of the wafer. After a final thermal sintering in the forming gas ($N_2$ with 4% $H_2$), the detectors were ready for testing. This process is currently under investigation.

## 2.2 Microstrip detectors

We tested, in collaboration with the COMPASS and LHCb experiments, a rejected half module of the 1994 DELPHI vertex detector [5]. The experiment was described in detail in [4]. The module consists of two AC coupled double sided silicon microstrip detectors with a sensitive area of 3.2 x 5.4 $cm^2$, daisy chained together and bonded to a double-sided hybrid. The $p^+$-sides of the detectors have strips with a pitch of 25 μm, with every second strip being read out. The $n^+$-sides of the detectors have strips with a pitch of 42 μm which run perpendicular to the $p^+$-side strips; the $n^+$-side strips are separated by $p^+$ blocking implants. The $n^+$-side signals are routed to the same short side of the detector plate where all bonding pads are located, using a second metal layer. The total number of strips in the module is 2560. The hybrid is equipped with ten MX6 CMOS analog readout ASICs with a shaping constant of 8 μs; these circuits are not radiation tolerant.

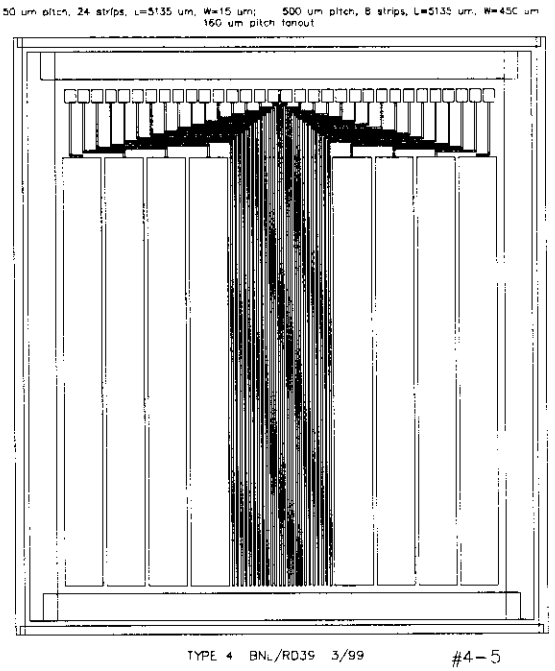


*Figure 1: The Beamscope silicon microstrip detector*

For the Beamscope prototype, which will be discussed in Section 4.3, a special Al/$p^+$/n/$n^+$/Al microstrip detector was designed and produced according to the process described above. The $p^+$-side (Fig. 1) has 24 strips of 5.135 mm length with 50 μm pitch and 15 μm width in the central region, plus 4 large strips of the same length with 500 μm pitch and 450 μm width on each side of the central region, and one active guard ring. The simple DC coupled design required only two masks in the production procedure thus reducing significantly the processing cost of the sensor.

## 2.3 Irradiation of the detectors

### *2.3.1 Neutron irradiations*

Irradiations of simple diode structures with neutrons were performed at the TRIGA nuclear reactor of the Jozef Stefan Institute in Ljubljana. Samples were irradiated in the experimental channel positioned in the reactor core. The spectrum of neutrons in the core has a range from thermal to fast (about 10 MeV) neutrons and was determined by threshold activation analysis [6] and independently by reactor core simulation. Calculations of NIEL (non-ionizing energy loss) in silicon from the measured spectrum were performed using damage functions from [7] and [8]. All neutron fluences and fluxes in this report are given as NIEL equivalent of 1 MeV neutrons (n/cm$^2$). The flux in the irradiation channel amounts to ~ $2 \cdot 10^{12}$ n/cm$^2$/s so irradiations to fluences in excess of $10^{15}$ n/cm$^2$ can be accomplished in less than an hour.

The fluence for individual samples was determined by gold activation converted to NIEL with the measured spectrum and damage functions. The systematic error on the fluence measurement is about 10 %. We shall report here results on sensors covering the fluence range of $1 \cdot 10^{14}$ - $2 \cdot 10^{15}$ n/cm$^2$.

### *2.3.2 Proton irradiations*

The DELPHI microvertex detector tip was irradiated at room temperature with 24 GeV protons at the CERN PS, in collaboration with the LHCb experiment. During irradiation the detector was not biased. The fluence was determined by measuring the activation of aluminum. The irradiation profile was inhomogeneous (see Section 4) and reached a maximum fluence of $3.5 \cdot 10^{14}$ p/cm$^2$ corresponding to an equivalent fluence of $1.9 \cdot 10^{14}$ n/cm$^2$. This detector drew a total current of 1 mA at 65 V at room temperature after irradiation, and it was operated at cryogenic temperatures in the SPS test beam as described in Section 4.

Silicon pad detectors with Al/$p^+$/n/$n^+$/Al structure were irradiated, in collaboration with the NA50 experiment, with 450 GeV protons of the SPS while keeping them at a constant

temperature of 83 K and biased. The detectors were irradiated and measured in a continuous-flow liquid nitrogen cryostat equipped with thin windows. The detector signals were read out, at lower beam intensity, with a charge amplifier having a shaping constant of 2 μs placed just outside the cryostat. The preliminary results are reported in Section 3.3.

In order to obtain a complete *in situ* measurement of the radiation damage when irradiating at cryogenic temperature, a special beam configuration was needed. During the irradiation phase the high intensity proton beam of the NA50 experiment was focused on the pad detector. Using a wire chamber just before the cryostat the beam size was adjusted to approximately match the pad area. The pad was then irradiated at maximum intensity (few $10^{10}$ p/burst) for some hours until $2 \cdot 10^{12}$ protons were accumulated. This corresponds to an equivalent dose step of about $10^{14}$ p/cm$^2$ given at a dose rate of about 1 Mrad/hour. At this point the beam intensity was lowered to $10^5$ p/spill of 300 GeV by inserting an aluminum target 118 m upstream of the detector, thus generating a secondary beam. This beam was much wider and was used for the measurement of the CCE. These two steps were repeated until the maximum dose of about $1.2 \cdot 10^{15}$ p/cm$^2$ was reached. This would in turn correspond to a 1 MeV neutron fluence of about $6 \cdot 10^{14}$ n/cm$^2$ [9]. This conversion however is based only on extrapolation, since no damage conversion factors for particles of such high energy are available in the literature.

### *2.3.3 Lead-ion irradiations*

Using the same arrangement discussed above, similar pad detectors were also irradiated operated at 83 K with the 158 GeV/nucleon high-intensity lead ion beam of the CERN SPS. The beam was steered and focused onto one of the pads of the detector. The beam intensity could be adjusted between $10^5$ and $10^8$ ions/burst; the burst duration was 5 s and interval 12 s. The detectors accumulated a total dose of about 1 Grad.

The prototype Beamscope tracker was exposed to the 40 GeV A lead ion beam of the SPS. During this run the microstrip detectors described above received a total dose of about 1 Grad.

In both cases, with 200 V bias voltage, the detectors showed no sign of signal deterioration. It is worth stressing however that in this case the signal is mainly determined by plasma effects than by the CCE. The estimation of the Pb ion damage constant is in progress, basing on the room-temperature leakage current density of the sensor and on NIEL simulation.

## 3.1 Diode junction detectors irradiated at room temperature

The devices investigated in [3] were DC-coupled Al/$p^+$/n/$n^+$/Al implanted silicon discussed above. In particular we tested structures with a sensitive area of 5 x 5 $mm^2$ having various thicknesses. The samples were irradiated at room temperature with different neutron fluences. The detectors were tested using Minimum Ionizing Particles (MIPs) from a radioactive source and a charge amplifier with 1 μs shaping constant. It is worth mentioning that in our investigation the CCE is calculated comparing the most probable value of the signal height of the irradiated detector with that of a similar but unirradiated detector. If the spectrum could not be properly fit by a Landau distribution, the measurement was rejected. A typical spectrum obtained with a detector irradiated up to $1 \cdot 10^{15}$ n/$cm^2$ is shown in Fig. 2.

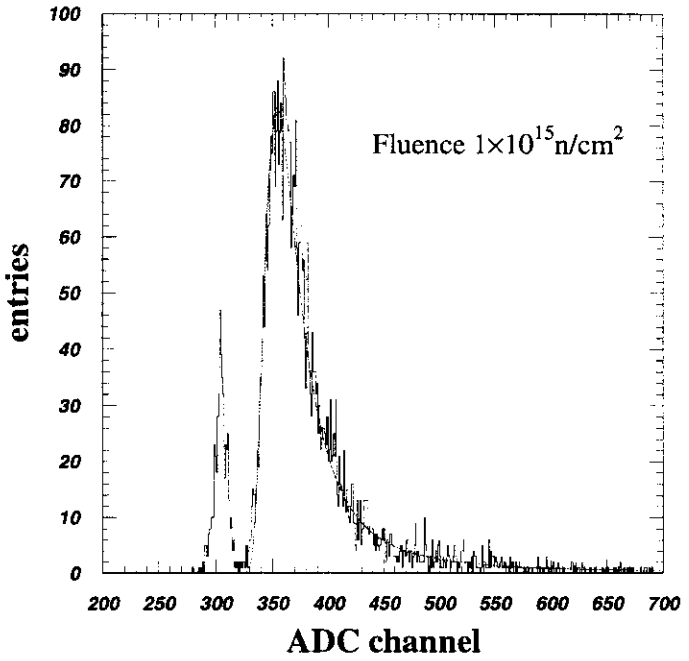


*Figure 2: A typical charge distribution obtained from a detector irradiated up to a fluence of* $10^{15}$ *n/cm*$^2$ *operated at 77 K under 250 V reverse bias.*

In agreement with the results of the ROSE collaboration [9] the leakage current is strongly suppressed by reducing the temperature. In particular, at 77 K the reverse leakage current is negligible for all detectors (less than 1 nA) up to a voltage of 250 V. Such a low current is observed in the case of detectors irradiated above $5 \cdot 10^{15}$ n/$cm^2$ also under forward bias since the bulk material behaves as a resistor of very high value. This allows operation of highly irradiated detectors irrespective of the bias polarity.

### *3.1.1 Temperature dependence of the CCE under reverse-bias operation*

It is worth mentioning that in materials rich in deep-level traps (such as silicon after heavy irradiation), the history of the bias voltage plays a crucial role in the time evolution of the amplitude of the signal at cryogenic temperatures. For example, reversing the bias polarity generates a transient condition in the bulk, during which the radiation-induced electrical pulses are gradually reduced in amplitude, and change sign only after a few minutes. This process was originally observed in germanium detectors [10] and was called the "detector polarization". It is therefore important to prepare the detector always into stable conditions before modifying the applied bias voltage. Another common striking feature is that, under reverse bias, the CCE decreases with time, i.e. the measurements repeated some time after turn-on of the HV yield a monotonically decreasing CCE, which converges towards a stable value.

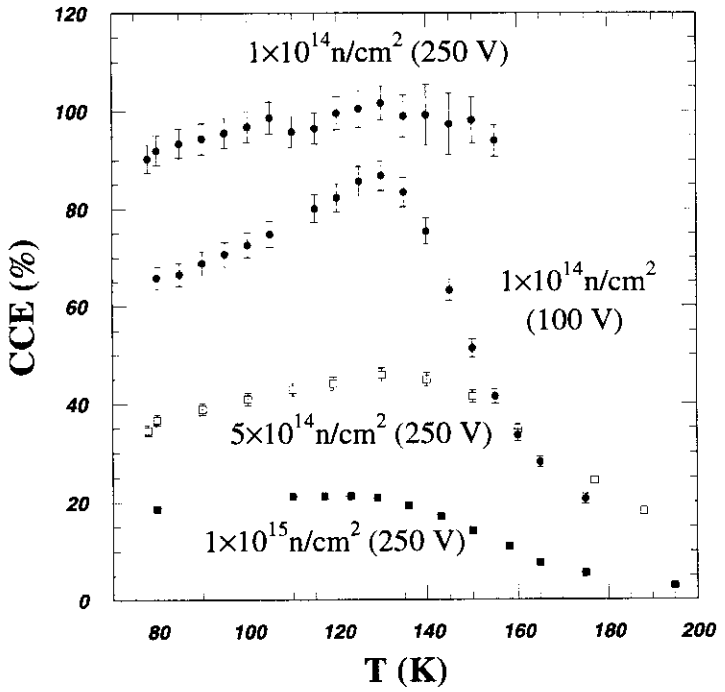


*Figure 3: Temperature dependence of CCE for three detectors irradiated with different neutron fluences operated at different bias voltages.*

The temperature dependence of all detectors shows some common features. The three detectors of Figure 3 are biased with a voltage such that at high temperature they are certainly not fully depleted. All detectors show very low CCE values in the high temperature range. A substantial rise of the CCE starts around 180 K, and the CCE reaches its maximum value at a temperature of around 130 K for all samples. The temperature of maximum CCE was found to be universal within the experimental accuracy. The decrease of the CCE observed below

130 K also has a universal character. The heavily irradiated detectors do not reach 100% CCE at the maximum applied bias voltage of 250 V; however, some recovery effect is still observable at low temperatures. The temperature scan in the case of the less irradiated detector has been also performed at 250 V. In this case the applied voltage is high enough to fully deplete the device even at intermediate temperatures, and the CCE is close to 100% at all temperatures at which the noise level allowed to perform measurements. This suggest that the non-linear increase in CCE due to operation at cryogenic temperature (known as the Lazarus effect) is a combination of reduced trapping and increased depletion.

### *3.1.2 Voltage dependence of the CCE under reverse-bias operation*

The voltage dependence of the CCE for a detector irradiated up to $10^{15}$ n/cm$^2$ measured at 77 K is shown in Fig. 4. Similar results have been obtained with other detectors irradiated with different fluences, with the exception of the maximum value reached.

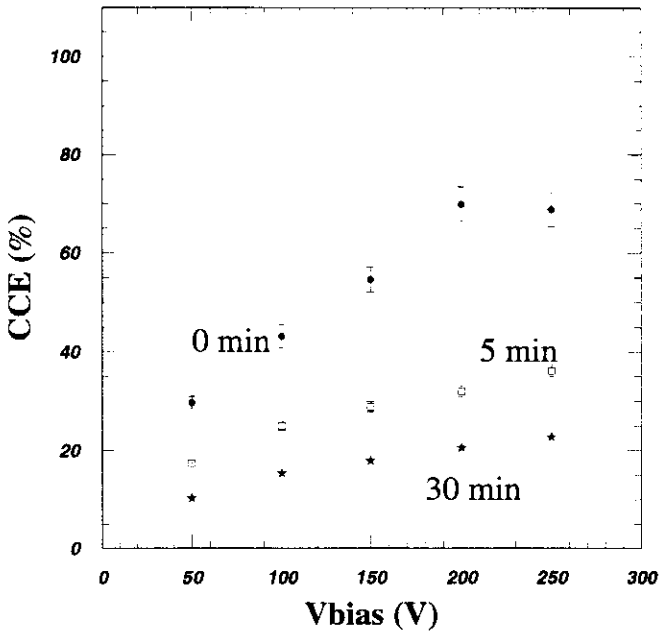


*Figure 4: Voltage dependence of the CCE of a detector irradiated up to $10^{15}$ n/cm$^2$ and operated at 77 K, measured at different time intervals after HV turn-on.*

The maximum CCE obtained immediately after applying the HV, shows a linear increase with the applied voltage up to around 70% at 200 V. However, due to the decay in time, for measurements taken at a given non-zero time after the HV is turned on, the slope of the CCE with the applied bias voltage is smaller. The stable CCE values match the poor results obtained for the CCE in the temperature scans.

### *3.1.3 Time dependence of the CCE under reverse-bias operation*

In order to understand better the time dependence of the CCE, the data of Fig. 4 are plotted in Fig. 5 as a function of time. The lines represent fits to exponential time dependence with time constants around 5 min. It can be seen that, as a general trend, the larger the applied bias voltage, the higher is the initial CCE value and the slower it decreases. Most of the CCE loss takes place in the first five minutes after the HV is applied. It is also important to note that in the case of detector irradiated up to $10^{15}$ n/cm$^2$ it is possible to completely suppress the time dependence of the CCE by means of a fairly large bias voltage which corresponds to a strong overdepletion. A confirmation that this situation is stable comes from the data of Fig. 3, where the CCE measured at 250 V stays constant at 100% during the temperature scan.

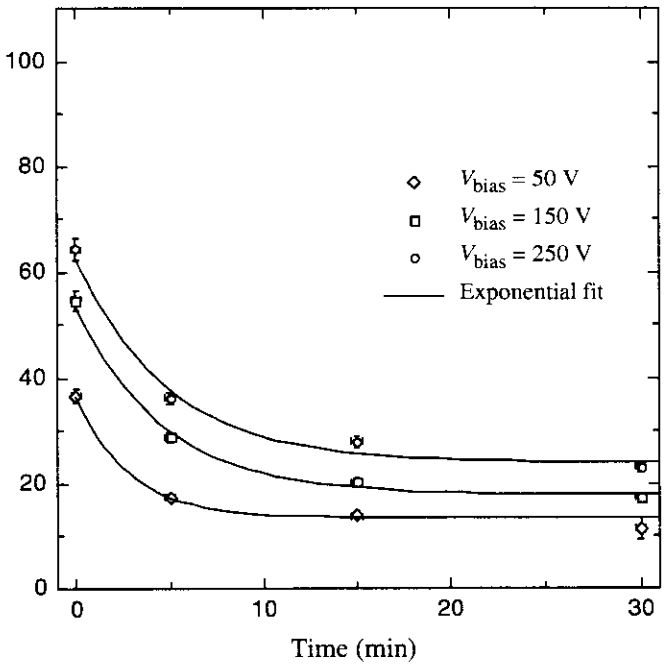


*Figure 5: Time dependence of the CCE of a detector irradiated up to $10^{15}$ n/cm$^2$ and operated at 77 K, measured at different reverse bias voltages.*

### *3.1.4 Light illumination under reverse-bias operation*

The second set of experiments consisted of illuminating the detector using light sources of various wavelengths in order to enhance the steady state current by means of optically generated non-equilibrium carriers. This was done in order to fill the radiation-induced traps and to achieve a better penetration of the electric field in the bulk material of the detector, as suggested in Ref. [11]. The intensity of the applied light was adjusted so that the leakage

current was about 5 nA, not adding a significant contribution to the overall noise of our measurement system. The main effect of the light illumination is that no time dependence of CCE is observed. Under reverse bias operation, illuminating with short wavelength light (yellow or green), results in the stabilization of the good values of CCE normally obtained immediately after switching on the HV without temporal decay.

### *3.1.5 Temperature dependence of the CCE under forward bias operation*

Forward bias operation has been considered very interesting for heavily irradiated silicon detectors, and promising results have already been obtained in the case of moderate cooling [12].

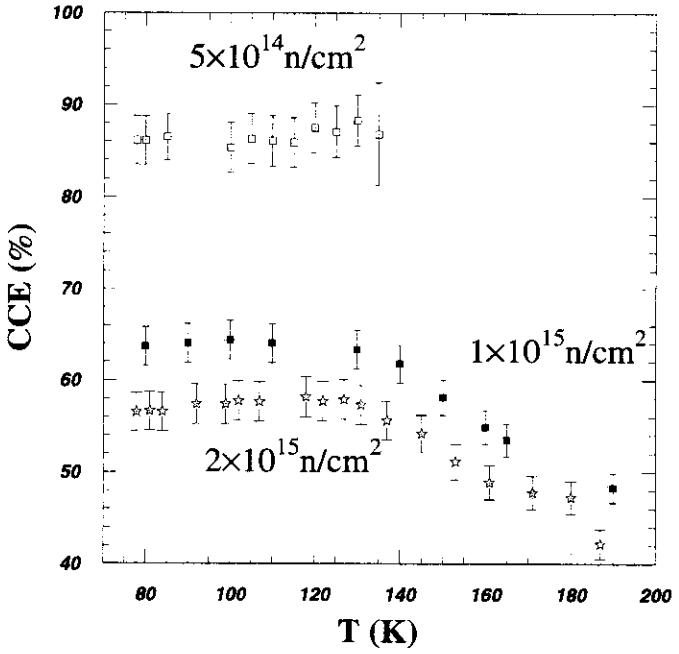


*Figure 6: Temperature dependence of the CCE for detectors irradiated with different neutron fluences operated at 250 V forward bias. Note that the zero of the vertical axis is offset in this plot.*

It is worth stressing, however, that in the case of cryogenic operation of heavily irradiated detectors, due to very high bulk resistivity, one cannot distinguish this mode from the conventional reverse bias operation, judging from the current passing through the detector. Moreover under this condition the CCE time decay is naturally suppressed.

The temperature dependence of the CCE under forward bias operation for detectors irradiated up to different neutron fluences is shown in Fig. 6. The CCE starts increasing around 180 K and saturates below 130 K, for all detectors. Measured values are about three times higher

than those observed under reverse bias. Moreover, good values of CCE start being recorded as soon as the temperature is low enough to allow performing the measurements. The observation of good CCE values for these relatively high temperatures is in good agreement with previous observations [12]. It is worth mentioning that the measurements are limited in the high temperature range by the large leakage current induced noise such that it was impossible to perform the Landau-fit.

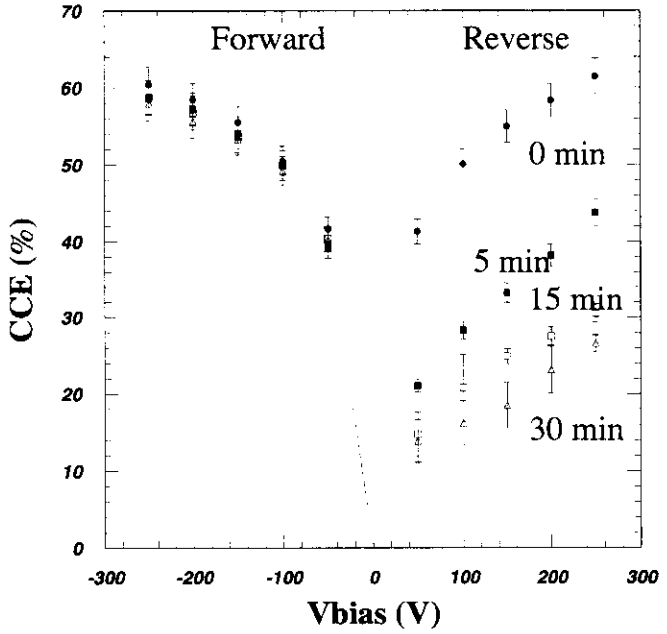


*Figure 7: Voltage dependence of the CCE of a detector irradiated up to $2 \cdot 10^{15}$ n/cm$^2$ and operated at 77 K, measured at different time intervals after HV turn-on in the extended voltage range allowed by the both reverse and forward bias operation.*

### *3.1.6 Voltage dependence of the CCE under forward bias operation*

The CCE is about three times higher with forward bias than with reverse bias in stable conditions, as shown in Fig. 7. These large values are the same of those observed under reverse bias immediately after switching on the HV since, under forward bias operation, the detector shows a time-independent CCE. This also correlates with the good improvement observed above in the case of the temperature dependence of the CCE.

### *3.1.7 Annealing effects*

The possible effects of the reverse annealing process on the CCE recovery were investigated on a sample irradiated up to $1 \cdot 10^{15}$ n/cm$^2$. The CCE was measured before and after an annealing period of about 1 year at room temperature over the full allowed bias range, as

shown in Fig. 8. No significant difference is found between these two sets of measurements. This suggests that the deep defects, which can be deactivated by means of operation at cryogenic temperatures, are formed during (or soon after) irradiation at room temperature, and are not seriously affected by the reverse annealing process

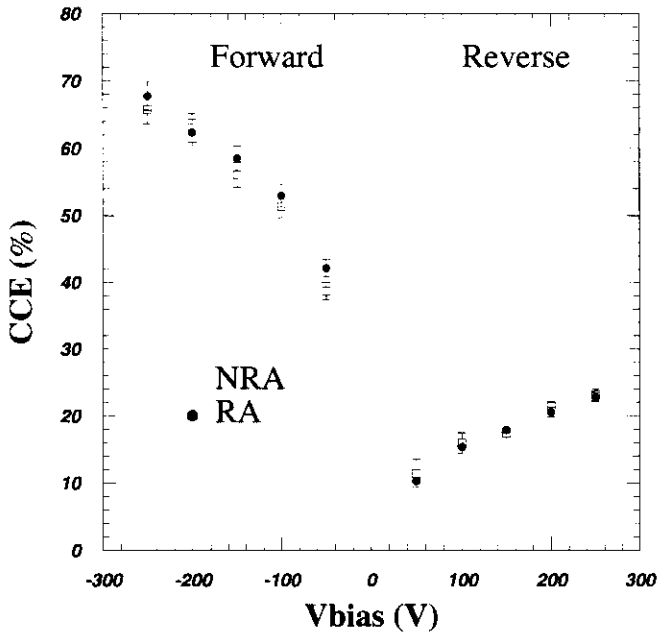


*Figure 8: Effect of reverse annealing on the voltage dependence of the CCE for detector irradiated up to $10^{15}$ n/cm$^2$. The measurements cover the full allowed voltage range including forward bias. At reverse bias only stable CCE values are plotted.*

### 3.2 The "double p" detector

After irradiation and bulk type inversion, a conventional $p^+/n/n^+$ implanted silicon detector still behaves like a diode, except that the junction develops from the $n^+$ implant instead of the $p^+$ implant [9], as shown in Figure 9. As discussed before, the CCE of such a diode, operated at cryogenic temperatures under reverse bias, degrades with time until it reaches a stable but reduced value. At these temperatures however, operation under forward bias is also possible, because then the detector bulk behaves like a large resistor limiting the equilibrium carrier current to negligible a value. In this case, the CCE does not depend on time and it stays at its initial high value. In order to get rid of the CCE time dependence, one could therefore think of using a standard diode detector under reverse bias until the resistivity of the type-inverted bulk, increasing with the accumulated dose, is large enough to enable operation under forward bias. Unfortunately this has the impractical drawback that bipolar electronics must be used to read out the detector signal and to supply the high voltage bias. Also, as discussed

before the detector bias current manipulation, by illumination with visible light, can remove the time decay of the CCE. However, this technique could prove unfeasible for large trackers.

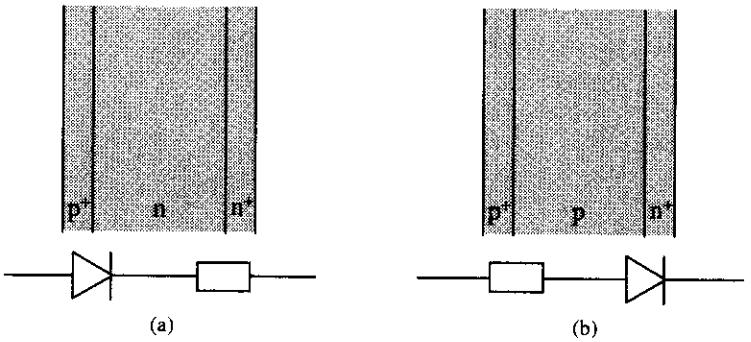


*Figure 9: Schematic representation of a standard Al/p⁺/n/n⁺/Al implanted silicon detector: (a) before and (b) after bulk type inversion due to radiation damage.*

Alternatively, one could consider the use of special devices designed to take full advantage of operation at cryogenic temperatures. We have investigated in particular a symmetric diode device: a $p^+/n/p^+$ implanted silicon detector. This type of detector can be considered as a series of two diodes connected in opposite directions. Below the breakdown voltage the detector never conducts whatever the polarity of the bias voltage, because there one of the diodes is always under reverse bias. After type inversion, it is expected that the detector does not have the double-diode characteristic any more, but behaves like a single resistor as shown in Figure 10. According to this scenario, one would expect the detector to have the following properties: the CCE is symmetric under forward and reverse bias, and after type inversion there is no decay of the CCE with time.

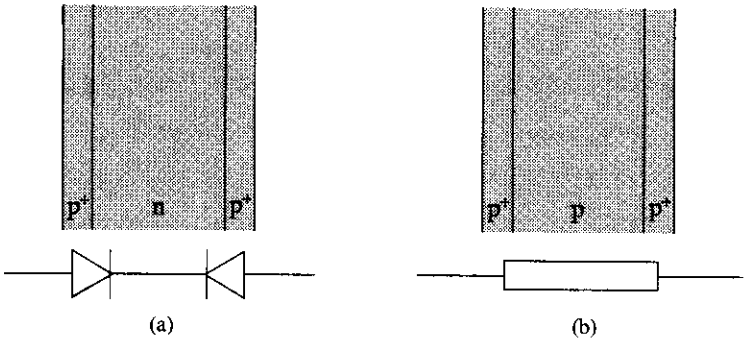


*Figure 10: Schematic representation of a symmetric Al/p⁺/n/p⁺/Al implanted silicon detector: (a) before and (b) after bulk type inversion due to radiation damage.*

The investigated $Al/p^+/n/p^+/Al$ sample is one of those discussed in Section 2.1. It has a sensitive area of 5×5 $mm^2$ and a thickness of 400 μm. It was irradiated with neutrons at room

temperature up to a fluence of $1\times10^{15}$ n/cm$^2$ which largely exceeds the bulk type inversion threshold [9].

### *3.2.1 Current-voltage characteristics*

Figure 11 shows the I-V characteristics of the investigated sample at room temperature. One can clearly see that the detector has a symmetric behavior. The current is of the same order of magnitude as the current measured for a standard Al/p$^+$/n/n$^-$/Al silicon detector under forward bias (~ 0.2 mA at a voltage of 10 V) irradiated to a comparable dose [3]. Also in this case, the leakage current is less than 1 nA up to 500 V at 77 K.

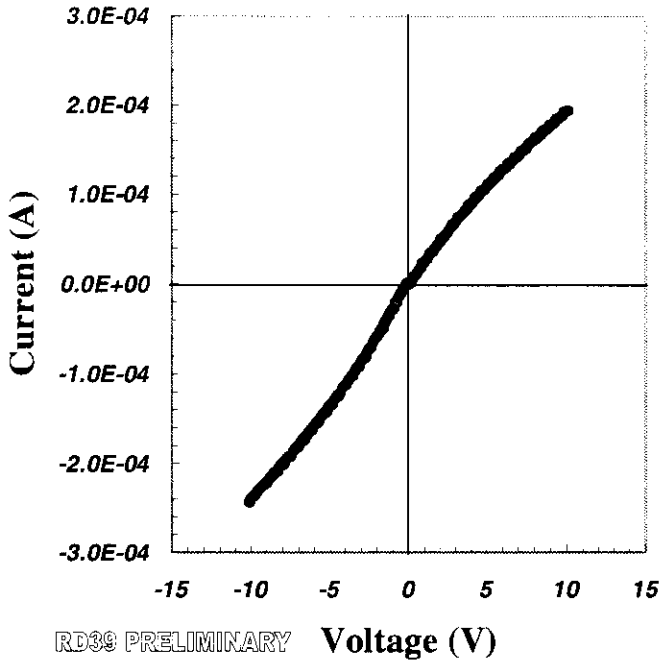


*Figure 11: I-V characteristics of the irradiated Al/p$^+$/n/p$^+$/Al sample measured at room temperature.*

### *3.2.2 Voltage dependence of the CCE*

The CCE was measured at three different temperatures; the results are shown in Fig. 12 as a function of the applied bias voltage. The values shown in the figure correspond to the stable values of the CCE (30 minutes after voltage turn-on).

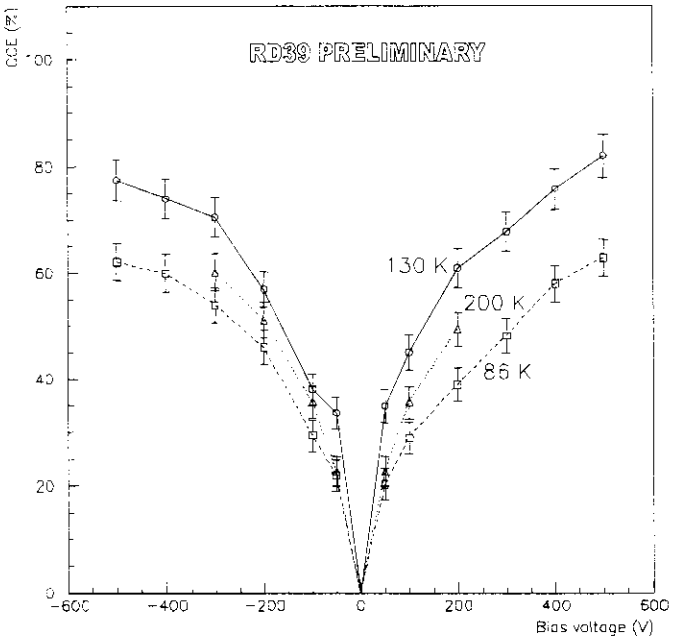


*Figure 12: The CCE of the irradiated Al/p⁺/n/p⁺/Al sample versus bias voltage at different temperatures. All measurements are taken 30 minutes after bias voltage turn-on.*

The plot clearly shows the expected symmetry of the sample for positive and negative applied bias voltage. The CCE increases with the absolute value of the applied bias voltage. Different values were obtained at the three different temperatures. Nevertheless, a maximum CCE of $84 \pm 4$ % is achieved at ±500 V and $T = 130$ K in agreement with previous experimental observations. At $T = 200$ K and bias voltages larger than +200 V or –300 V the large leakage current affected the measurement such that it was impossible to fit the data with a Landau distribution. In these measurements it was possible to extend the applied bias voltage above the previous limit of 250 V, enabling us to see the increase of the CCE with the applied voltage beyond the previous range.

### *3.2.3 Time dependence of the CCE*

The results of the CCE measurements as a function of time at 86 K for several positive and negative bias voltages show that the CCE is still dependent on time, which was not expected. Clearly, the device does not have a completely ohmic behavior, but it rather "remembers" that it was a double diode before irradiation. At 500 V the CCE decays $8 \pm 1$ %, while at 50 V the decay is $13 \pm 1$ %: the time dependence clearly decreases with increasing bias voltage.

In Figure 13 the CCE versus time is shown for a fixed bias voltage (500 V) and several temperatures. From this plot one can conclude that the decay of CCE becomes smaller at higher temperatures: at 200 K there is basically no time dependence any more.

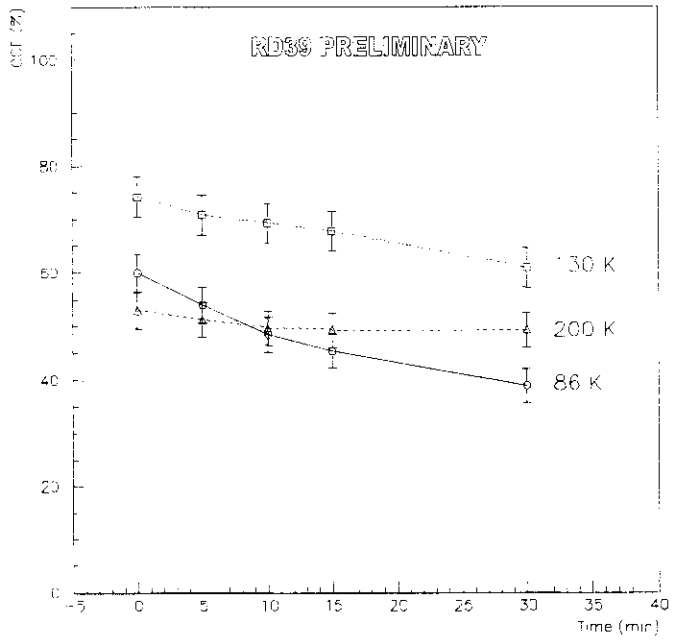


*Figure 13: The CCE of the irradiated Al/p$^+$/n/p$^+$/Al sample versus time after voltage turn-on. The measurements were taken at a bias voltage of 200 V for three different temperatures.*

In summary, at a given temperature the CCE shows a decay with time which is smaller for larger bias voltages. For a given bias voltage, the decay becomes smaller at higher temperatures. When the symmetric detector is compared to a standard detector in reverse bias, the time dependence turns out to be much smaller for the former. For comparison, the CCE of the standard detector at 200 V decays from an initial value of ~ 60 % to ~ 20 % in 30 minutes. At the same bias voltage and in the same period of time, the CCE of the Al/p$^+$/n/p$^+$/Al detector decays from ~ 60 % to ~ 40 %. It is worth noticing that at 500 V the CCE of the symmetric detector does not decrease below 60 %. This difference in time dependence cannot be attributed to the difference in temperature at which the measurements were taken since, as can be derived from Fig. 5, between 77 K and 86 K the CCE of a standard detector changes less than 2 %.

### *3.2.4 Influence of the preamplifier shaping time constant*

In the case of the double p detectors, all the CCE measurements were taken with two different preamplifier shaping time constants of 1 μs and 0.25 μs, in order to investigate any influence of the charge transit time on the collected charge. In Figure 14 the results are shown in the case of operation at 130 K (optimal temperature).

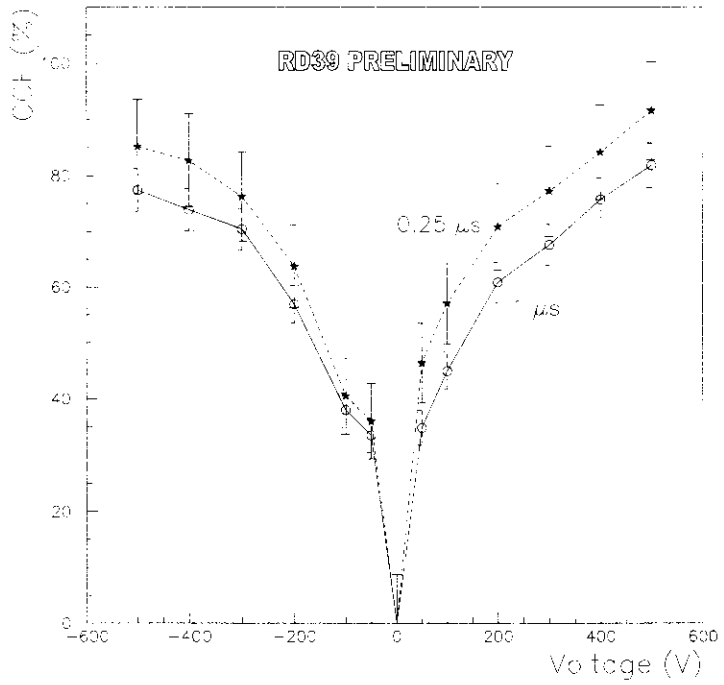


*Figure 14: CCE versus bias voltage at 130 K for two different signal shaping times. The measurements were taken after 30 minutes.*

As one can see, both shaping times give the same value for the CCE within the deviation intervals. Measurements under other circumstances (i.e. different temperatures and time intervals after voltage turn-on) give the same result. These results verify that the charge transit time is fast enough for the signal to be amplified with a shaping time of 250 ns.

## 3.3 Diode detectors irradiated *in situ* at cryogenic temperatures

Though, as discussed above, several studies have proved the radiation tolerance of silicon detectors operated at cryogenic temperatures, following room temperature irradiation, no previous investigations have been made on the behavior of detectors irradiated *in situ* at low temperatures. The devices investigated here were DC-coupled Al/$p^+$/n/$n^+$/Al implanted silicon pad detectors processed and irradiated in the SPS proton beam as discussed in Section 2. In

particular we tested structures with a sensitive area of 1.5 x 1.5 $mm^2$ having a thickness of 400 μm.

As was described in Section 2.3, the pad detector was irradiated in steps to the dose of about $1.2 \cdot 10^{15}$ $p/cm^2$ in the 450 GeV proton beam at the CERN SPS, equivalent approximately to a 1 MeV neutron fluence of about $6 \cdot 10^{14}$ $n/cm^2$ [9] based on extrapolation of existing data. The CCE was measured using a special low intensity beam configuration. Also in this case, if the signal spectrum could not be fitted by a reasonable Landau spectrum, we rejected the measurement.

### *3.3.1 Current-voltage characteristics*

The current-voltage characteristics for the irradiated pad under reverse bias was measured with polarizing the guard-ring at the same voltage of the pad in order to measure only the bulk current. The maximum applied voltage was 500 V. Figure 15 shows the I-V characteristic at 300 K for the irradiated pad. As shown in the inset of Figure 15, the leakage current is dominated by the generation component, which is found to be proportional to the square root of the bias voltage, as expected. At 83 K the leakage current was less than 1 nA up to 500 V.

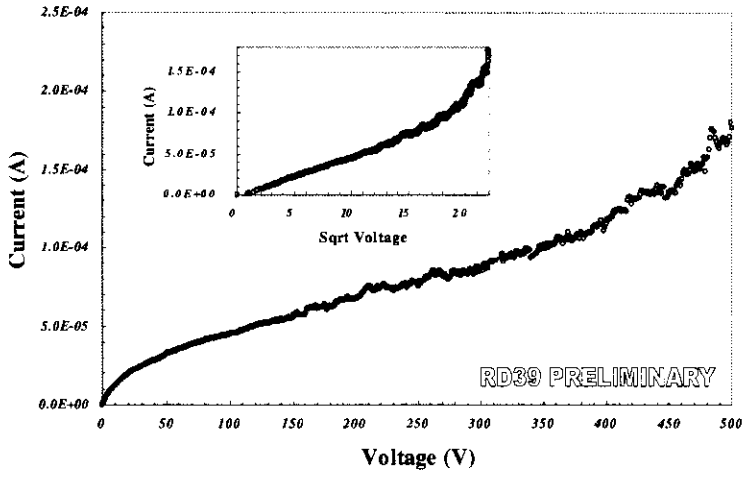


*Figure 15: Current–voltage characteristic measured at 300 K under reverse bias for the pad detector irradiated up to $1.2 \cdot 10^{15}$ $p/cm^2$. The inset shows the linear relationship between the current and the square root of the voltage.*

### *3.3.2 Voltage dependence of the CCE under reverse bias*

The CCE has been normalized to that before the irradiation, which reaches 100% CCE at 50V, as shown in the Figure 16. Also in this case, each measurement was performed after the detector had been left unbiased for a few minutes, to allow de-polarization. Then, after having biased the detector, the time evolution of the CCE was monitored.

At 100 V, starting from 100% CCE for zero dose, the CCE is seen to decrease to 80% at $3 \cdot 10^{13}$ p/cm$^2$ and to 50% at the fluence of $1.2 \cdot 10^{15}$ p/cm$^2$. At this dose, further increasing the bias voltage up to 200V results in a maximum CCE of 65%. The CCE varies linearly with voltage within this range, suggesting a higher value of the CCE for higher bias voltage.

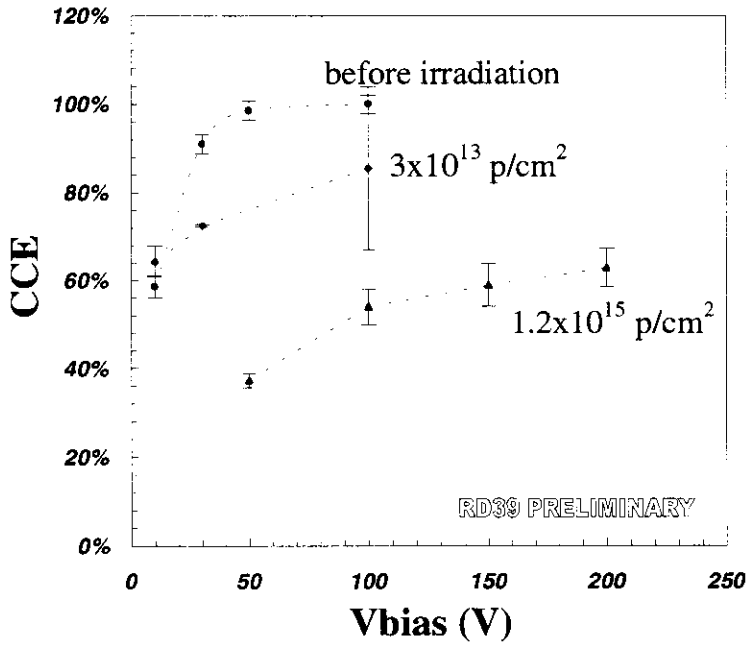


*Figure 16: Bias voltage dependence of the CCE of the irradiated pad detector for different accumulated fluences. The measurements are taken immediately after applying the bias voltage.*

### *3.3.3 Time dependence of the CCE under reverse bias*

It is interesting to note that at 200 V reverse bias a time evolution of the CCE takes place for accumulated fluences above $6.5 \cdot 10^{14}$ p/cm$^2$. This effect, though only slightly evident at $1.2 \cdot 10^{15}$ p/cm$^2$, is more clear after a partial annealing was made at the end of the experiment. For this, after the maximum irradiation dose was achieved, the detector was warmed above 200 K, and was left at this temperature for around 1 hour before cooling it back to 83 K and measuring the CCE which is shown in Figure 17.

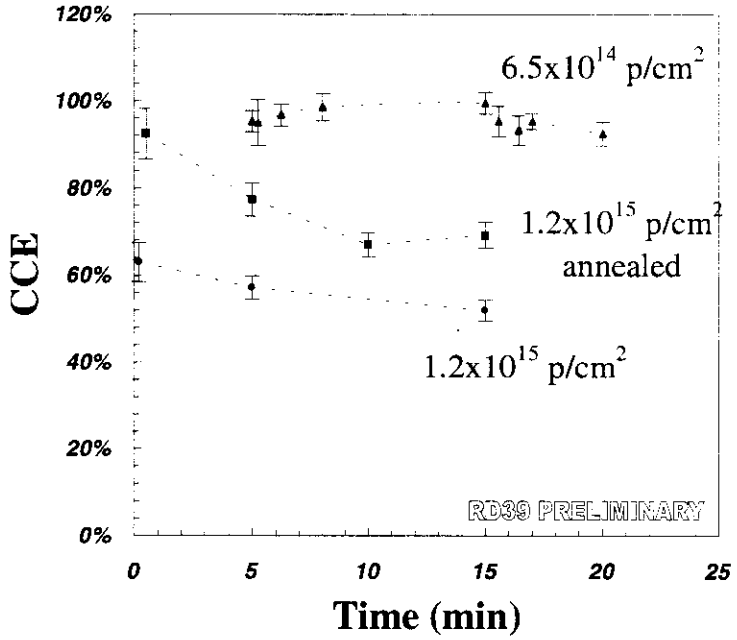


*Figure 17: Time evolution of the CCE of the irradiated pad detector for different accumulated fluences. The bias voltage is 200 V.*

### *3.3.4 Annealing effects*

The previously discussed warming cycle was introduced to check the role of short term beneficial annealing. Despite being well know [9], this type of annealing cannot in fact be easily characterized when irradiating at room temperature since it takes place continuously during the irradiation process. This is not clearly the case when irradiating at cryogenic temperature since the lattice thermal energy is reduced substantially. At the maximum fluence, after the beneficial annealing took place, a recovery of CCE up to 80% at 50V bias was observed. A further increase of the bias voltage to 200 V results in a CCE value of 95%. It is worth noticing that this increase in CCE due to beneficial annealing is supposed to quickly disappear when the detectors are held for a long time at room temperature (reverse annealed), and measurements to verify this are currently in progress.

## 3.4 Modeling of the Lazarus effect

The previously discussed results can be qualitatively interpreted in the framework of the present understanding of the filling of deep-level radiation-induced traps. These traps play an important role for the CCE at cryogenic temperatures, as was already suggested in Ref. [11].

It is well known [13] that the conductivity of heavily irradiated silicon detectors is related to the deep-level defects, rather than to the shallow-level dopants as in the non-irradiated

material. As a result, already at room temperature the non-depleted region of a diode has a resistivity close to that of an insulator, after the material has undergone type inversion. In this case, the non-sensitive layer of the detector acts as a capacitive divider, which reduces the signal collected at the electrodes. The signal measured in a detector of total thickness $D$ is then proportional to $Q \cdot d/D$, where $Q$ is the total charge generated in the active layer of thickness $d$. In the case of a MIP, where $Q$ is proportional to $d/D$, one expects a charge collection efficiency which behaves as $(d/D)^2$.

The CCE also depends on charge trapping [10, 14]. If the electrons and holes generated by ionization are trapped during their drift, some fraction of the signal is lost, and the CCE is less than 100% even for a fully depleted detector. Consequently, the CCE can be qualitatively expressed as:

$$CCE \propto \left(\frac{d}{D}\right)^2 \exp\left(-\frac{t_{drift}}{\tau_{trap}}\right), \tag{1}$$

where $t_{drift}$ is the drift time of the excited carriers, and $\tau_{trap}$ is the trapping time constant related to the radiation-induced deep levels. The thickness $d$ of the active layer for an under-depleted detector depends on the applied bias voltage $V$ and on the space charge density $N_{eff}$ according to the relation:

$$d = \sqrt{\frac{2\varepsilon\varepsilon_0 V}{e|N_{eff}|}}. \tag{2}$$

All samples of the present study were n-type irradiated beyond space charge sign inversion, and the $N_{eff}$ at room temperature is therefore negative. When the temperature decreases, the emission process is drastically suppressed due to the exponential dependence of the emission time constant $\tau_d$ on temperature:

$$\frac{1}{\tau_d} \propto \exp\left(-\frac{E_t}{kT}\right), \tag{3}$$

where $E_t$ is the trap energy and $k$ the Boltzman constant. It is worth reminding that this effect is important only for deep traps in the silicon band gap, for which $E_t$ is of the order of ~ 0.5 eV, while it is less pronounced for very shallow defects.

The very long emission time, caused by the reduced lattice thermal energy, has in fact a double effect. The trapping/emission process is strongly unbalanced, leading to filling of a significant fraction of deep levels which reduces $|N_{eff}|$ until it finally reaches a value near zero. This reduction of $|N_{eff}|$ leads to an increase of $d$ and consequently of the CCE for a given bias

voltage below full depletion. Moreover, the filled traps do not capture any more the radiation-induced carriers, thus contributing as an additional beneficial effect in the trapping term. In such a way, improvements in the CCE can be achieved due to both factors in Eq. (1).

The trap filling process seems to reach a maximum effectiveness at a temperature of about 130 K, while the CCE decreases at lower temperatures for all detectors. Similar results have been obtained with the technique of laser filling, discussed in Refs. [11,15]. It is interesting to note that, in the case of the detector irradiated up to $10^{14}$ n/cm$^2$ measured at 250 V, no temperature dependence of the CCE was found. This could indicate, assuming that 250 V corresponds to full depletion, that there are no trapping losses due to reduced temperature. This interpretation is also compatible with the results obtained with the double-sided microstrip detector irradiated up to $10^{14}$ n/cm$^2$ that clearly show that the CCE recovery is associated with an increase in depletion depth.

The time dependence of the CCE at 77 K, shown in Figures 5 and 17 (see also Section 4), is a most striking phenomenon. The experimental procedure allowed to perform each measurement with the same initial filling status of the deep traps, and eliminated any accumulated charge in the detector bulk, possibly remaining from the previous measurement. The CCE degradation takes place in the first 5 minutes, and its absolute value does not depend on the applied bias voltage. Moreover, the initial value does not reach 100%. The data seem to indicate that just after HV turn-on, the detector behaves as if it were fully depleted. The CCE degradation with time could be related with the change in time of $N_{eff}$ and consequently of the geometrical factor due to the *d/D* ratio. The quantitative explanation of the data, however, requires accurate knowledge of the leakage currents and of deep trap concentrations for each detector.

Theoretical and experimental work, using different techniques, is in progress to clarify the microscopic modeling of the Lazarus effect in a wide range of fluences.

## 4 MICROSTRIP DETECTORS

The use of double sided strip detectors extends the amount of information from that was available from diodes alone, by allowing a measurement of the cluster shapes on both the ohmic ($n^+$) and junction ($p^+$) sides of the detector. Depending on the width of the depletion layer in the detector, the cluster shapes change significantly, due to the changes in the electric field penetration. As there is a well known relationship between incomplete depletion and drop in the CCE, the measured cluster shape provides a powerful cross check on the measured CCE. The use of the cluster shape to distinguish between cases of complete and incomplete depletion is particularly useful for the analysis of heavily irradiated detectors,

where the full-depletion voltage rises rapidly with the incident fluence and may not be well known for all situations.

### 4.1 CCE results of the DELPHI detector under reverse bias operation

The DELPHI detector module, built of double-sided sensors as described briefly in Section 2.2, was irradiated in the CERN PS. The irradiation profile was made inhomogeneous in order that the front-end readout ASICs would not get damaged. Judging from the CCE of the damaged regions of the detector, the dose distribution is illustrated as shown by Figure 18. The maximum fluence of $3.5 \cdot 10^{14}$ p/cm$^2$ was measured, as discussed in Section 2.3, on a 1 cm$^2$ spot in the middle of the black region of Fig. 18.

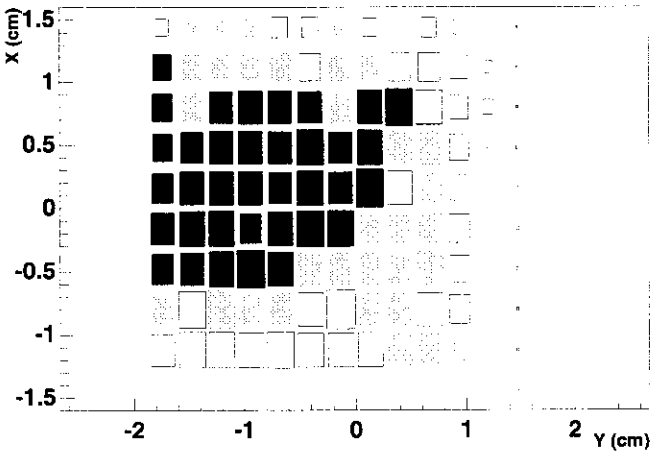


*Figure 18: A representation of the irradiated tip of the DELPHI module detector subdivided in the regions according to their CCE. The black area corresponds to the most irradiated region.*

The test of the irradiated DELPHI detector was performed in the 100 GeV/c muon test beam of the CERN SPS. Tracks were reconstructed using a COMPASS telescope consisting of 3 stations of silicon microstrip detectors. The irradiated module was placed in a cryostat together with a similar non-irradiated reference module. Throughout operation, the module was kept at temperatures ranging from 115 to 140 K. Except for one chip on the reference detector, and one low gain chip on the irradiated detector, the 18 remaining readout chips functioned normally, as expected for CMOS circuits [16]. After the beam-test it was found that, possibly due to repeated thermal cycling, about 50 bond wires out of a total of 1280 on the irradiated detector were detached.

Also in this case the general trend, discussed above in the case of the diode detectors, is confirmed. The CCE increases with the applied voltage and degrades with time, and the history of the bias voltage plays a crucial role. An example of time dependence of the CCE is shown in Fig. 19. An advantage in this case is, however, that the measurement of the cluster shapes on both the ohmic ($n^+$) and the junction ($p^+$) sides of the detector allows inferring the depth of the active depleted layer.

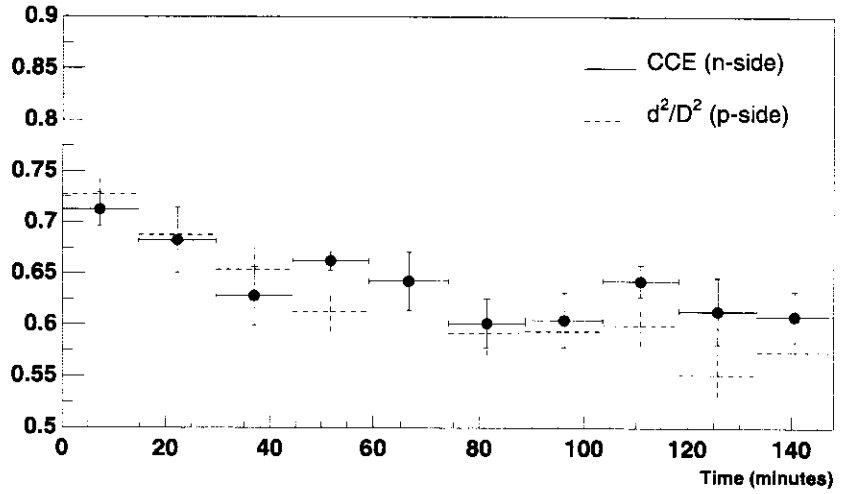


*Figure 19: CCE $n^+$-side (circles) and normalized depletion depth as a function of time for the highest irradiated region of the detector.*

In fact, in an irradiated silicon detector, which has undergone type inversion, the depletion region grows with the applied voltage from the ohmic ($n^+$) side of the detector. The non-depleted region reacts to an AC electrical signal like an insulator. During the first few ns after the passage of a particle, the electrons and holes resulting from interactions drift along the electric field lines in a direction perpendicular to the detector plane. On the $n^+$-side the field lines bend towards the implants, and the usual good track position resolution is easily achieved. On the $p^+$-side instead the charges stop drifting when they reach the non-depleted region. If the strip pitch is sufficiently fine with respect to the depth of the non-depleted region, this results in a significant spread of the resulting cluster which is illustrated in Fig. 20. Because of the limited S/N performance for MIPs, the cluster spread can seriously degrade the resolution.

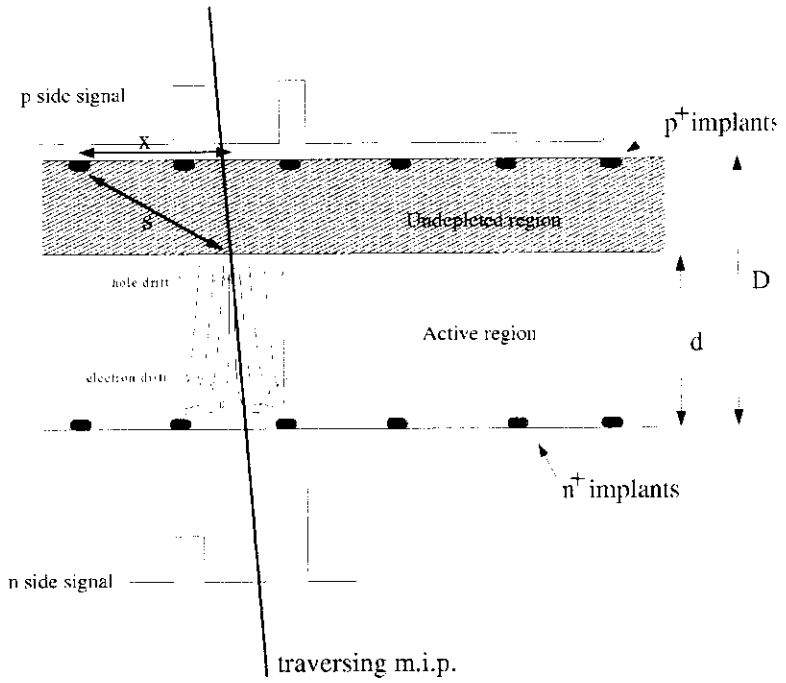


*Figure 20: Sketch of the charge distributions on the $p^+$- and $n^+$-sides of a microstrip detector.*

## 4.2 Position resolution of the DELPHI detector

The COMPASS test beam set-up provided three independent measurements of the position of a track per projection, thus allowing an unambiguous de-convolution of the resolution of the individual detectors. The experimental and simulation results are summarized in Figure 21. The resolution on the $p^+$-side of the reference detector was found to be around 5 μm, in agreement with the expectation for 25 μm pitch with every second strip read out. The resolution on the $n^+$-side of the reference detector was found to be 19 μm, as expected for 84 μm strip pitch and perpendicular tracks. The resolution on the $n^+$-side of the irradiated detector shows no dependence on the CCE. Since the S/N for full depletion was measured to be around 18, and the detector depletes from the $n^+$-side, this is as was expected. The measured value is around 12 μm, whereas one would expect around 9 μm for a detector with 42 μm strip pitch. The resolution on the $p^+$-side of the irradiated detector is 12 μm in the case of full depletion and worsens rapidly with decreasing CCE. The dotted curves show two Monte Carlo simulations for the resolution, made with a method outlined in the previous discussion on the increase in the cluster size due to incomplete depletion.

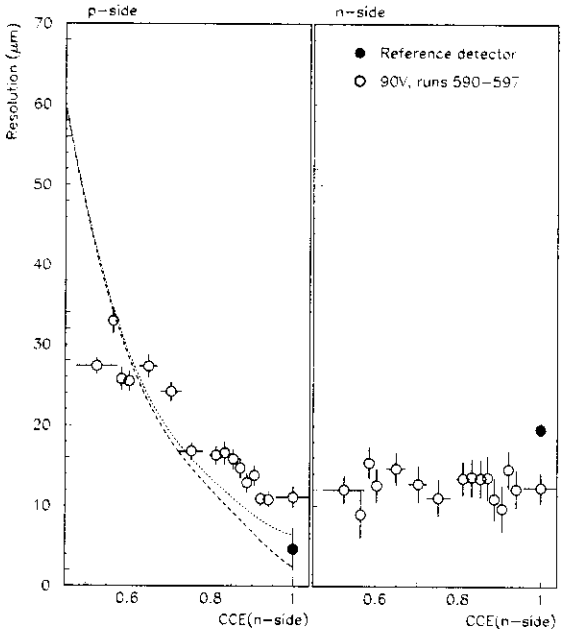


*Figure 21: Resolution for the $p^+$-side and the $n^+$-side, as a function of CCE ($n^+$-side). Note that the reference detector has a $n^+$-side pitch double that of the irradiated detector.*

It is worth mentioning that in the case of trackers operated in strong magnetic field, the increased mobility of the carriers due to the reduced temperature would lead to a significant change of the Lorentz angle. This in turn would affect the track position resolution. This effect is currently under investigation.

### 4.3 A prototype beam hodoscope for heavy ions

The prototype beam hodoscope (Beamscope) for fixed target heavy ion experiments such as NA6i [17] is the first application of radiation hardened silicon detectors based on the Lazarus effect. Such experiments require the detection and tracking of every lead ion in the beam with position resolution of ~ 10 μm, triggered by a delayed signal from another subdetector. The Beamscope should work at beam intensities of the order of $10^7$ ions/burst (5 s), and the total expected accumulated dose would reach 100 Grad in one period of operation.

Based on the previously discussed encouraging results on silicon microstrip sensors, a detector with 50 μm pitch, operated at 130 K, was chosen as a sensor for the Beamscope prototype. The sensor design, which includes also wide strips for beam steering, was described in Section 2.2 and is illustrated in Figure 1. The wide detector strips were connected to current-to-frequency converters located outside the cryostat. The frequencies produced by these converters were proportional to the rate of the lead ions traversing the

strips, and were recorded by means of CAMAC scalers. This information was used for coarse beam steering and was found to be very efficient.

The detectors were mounted in a special cryogenic PCB described in Section 5 (see Figure 22) and were placed in the vacuum chamber of the continuous-flow cryostat which is also discussed in Section 5.

The readout chain is shown in Figure 23. The narrow detector strips and the backplanes were connected via 100 Ω microstrip transmission lines on the PCB to fast amplifiers, located on four printed boards outside the cryostat. The lines were terminated on both ends with matched loads. AC-coupling was used for the backplane signals. The amplified signals were connected to discriminators with programmable threshold (six CAMAC modules LeCroy 4416). The amplified backplane signals were also sent to a digital scope (LeCroy LC584).

The discriminator signals of the narrow strips were used for tracking, and were also counted by means of CAMAC scalers. For the tracking, the occurrences of the signals during the last 3.4 μs was stored in a multi-hit time recorder system (MHTR), which covered by far the delay of the zero degree calorimeter trigger, used for this test. The MHTR system, which consists of 12 CAMAC modules, was designed and built specially for this experiment by the Bern group. The MHTR system did not require any computer intervention during the beam spill, since the data was transferred and buffered in a CAMAC memory module (LeCroy 4302).

The operation of the MHTR is based on digital sampling of the discriminator signals. This is performed by EPLDs, which are clocked at 150 MHz. An interleaved sampling technique is implemented, which increases the effective sampling rate to 600 Ms/s, i.e. to one sample every 1.67 ns. The sampled signal of each microstrip is stored in a circular buffer for 3.4 microseconds, being continuously overwritten after this time. The arrival time of the trigger signal is determined with same interleaved sampling technique, i.e. with the same digital resolution of 1.67 ns as for the microstrip signals. The content of the circular buffers is frozen after the arrival of a trigger signal. Then the data reduction and read-out logic calculates the time differences of the stored strip signals with respect to the trigger signal, encodes it together with the channel number in a appropriate way and transfers the data to the buffer memory module. Strong data reduction can be achieved, especially for high beam intensity, by accepting only hits in a time window corresponding to the trigger delay.

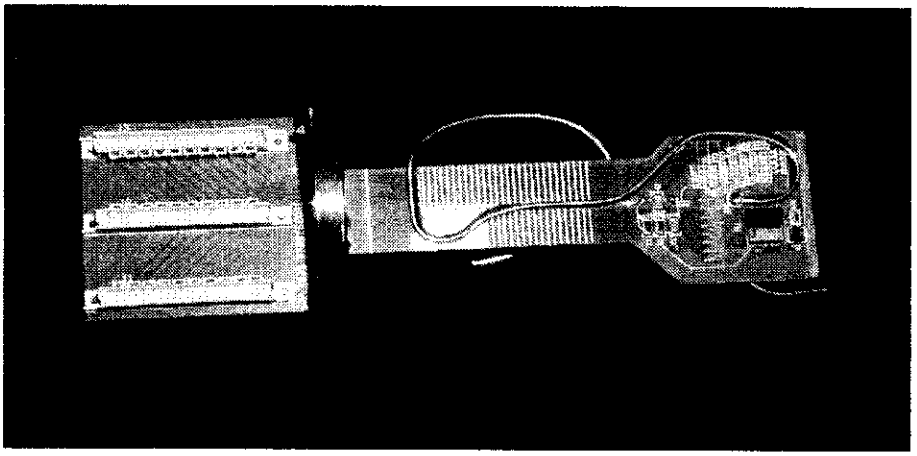

*Figure 22: The Beamscope PCB containing two detectors mounted back-to-back and rotated 90 degrees.*

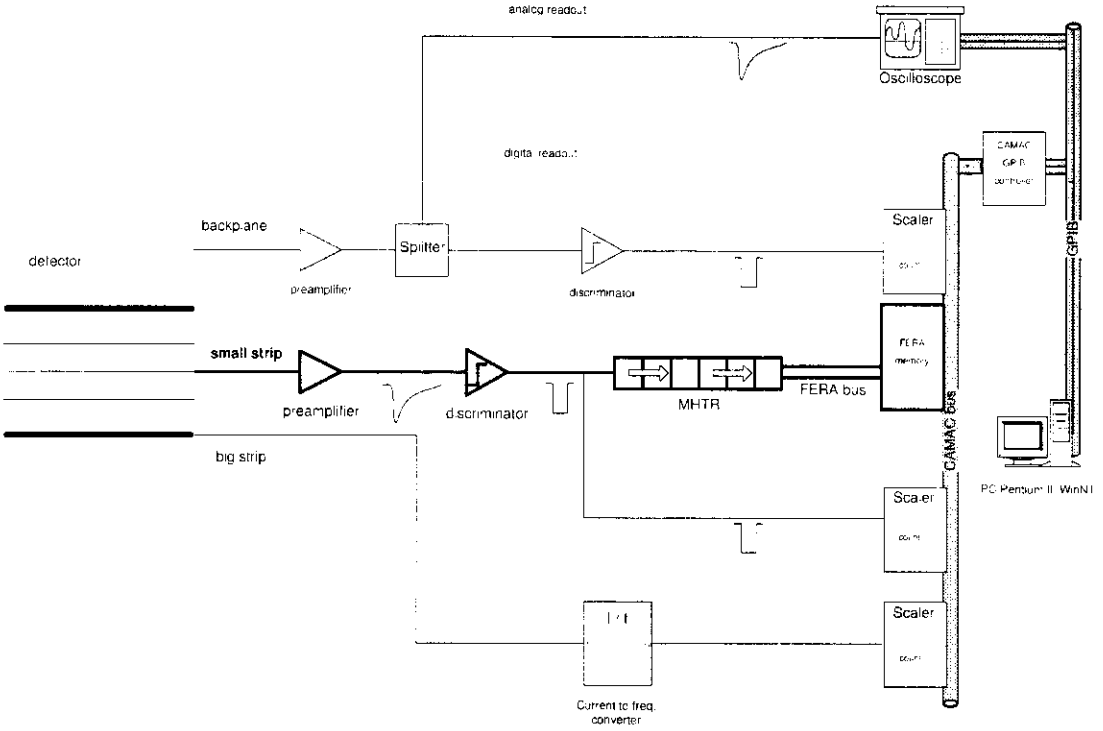


*Figure 23: Schematic of the DAQ and Slow Control.*

During October and November 1999, the Beamscope system was installed in front of the NA50 experiment (see Fig. 24) and performed very well in two test beam runs.

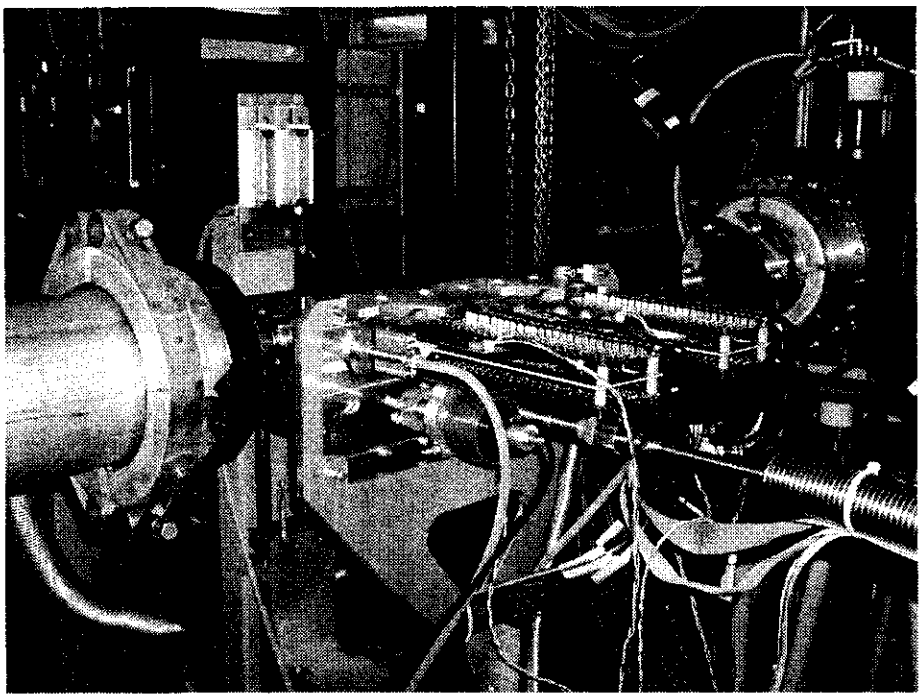

*Figure 24: The Beamscope installed in front of the NA50 experiment.*

Online monitoring based on scaler data was used for beam steering. An impressive image of the horizontal beam profile with unprecedented spatial resolution is shown in Fig. 25. In a relatively short time we have taken enough data for pulse and time correlation analysis. Some of the preliminary results obtained so far are presented below.

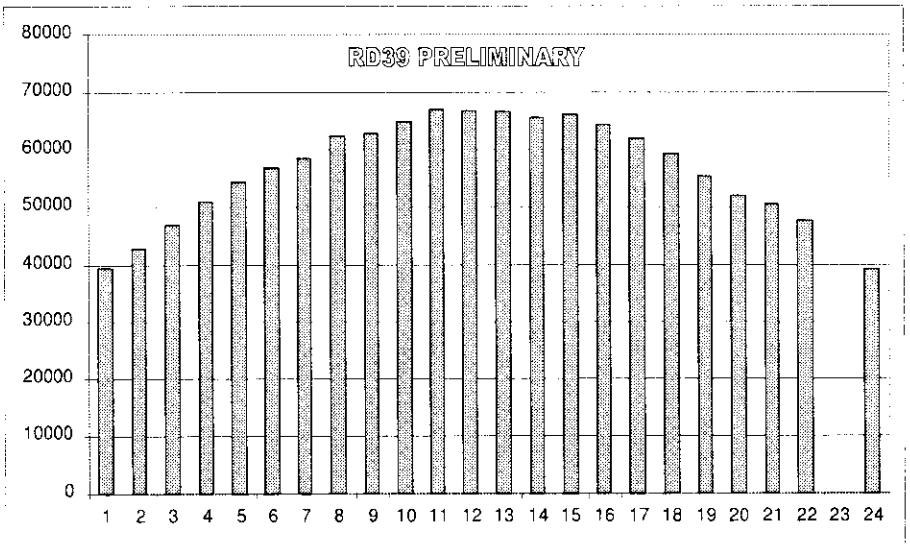


*Figure 25: The horizontal profile of the SPS ion beam as seen by one plane of the Beamscope. Note that the strip pitch is 50 μm. The 23rd strip was defective.*

The backplane signal was high enough (up to 200 mV for 200 V bias voltage) to be read even without preamplifiers, in that case, very short rise time (< 0.5 ns was observed); this time is determined by the amplifiers rather than the charge transit time. A typical pulse acquired directly at 8 GS/s for 50 V bias voltage is shown in Fig. 26, illustrating the rise time and the long tail of the signal. Shapers were introduced to reduce the long (~ 20 ns) tail. This backplane signal, in coincidence with the backplane signal of the sensor with diagonal strips, can be used for triggering the detector readout. The timing characteristics of these signals are better than those of scintillators, in particular if a faster amplifier is used.

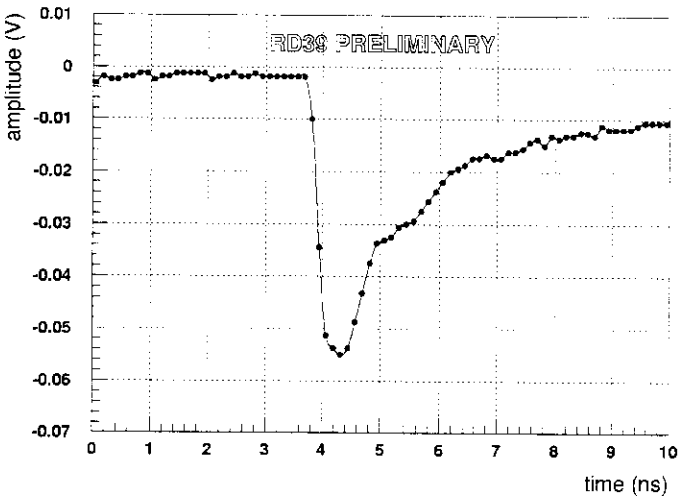


*Figure 26: Backplane analog signal (unshaped).*

Preliminary offline analysis indicates good data quality and a good overall behavior of the Beamscope during the test beam run. The distribution of delays between the crossing of a Pb ion on a silicon detector and the arrival of the ZDC trigger from NA50 is shown in Fig. 27, at 1.7 ns wide time bins. The very narrow peak indicates a very precise timing and can be used for an efficient selection of beam particles.

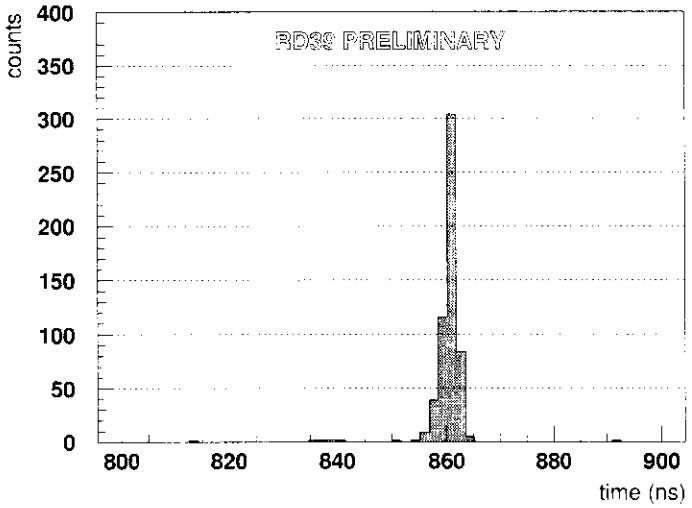


*Figure 27: Time distribution of the hits in one microstrip detector in respect to the ZDC triggers.*

Finally, the good correlation between strip hits (Fig. 28) shows a slight misalignment between detector planes 1 and 2 corresponding to a deviation form the diagonal crossing the origin. Given the widths of the small strips, the misalignment corresponds to about 500 μm across 20 cm, that is, to a horizontal angular offset of 2.5 mrad with respect to the beam axis.

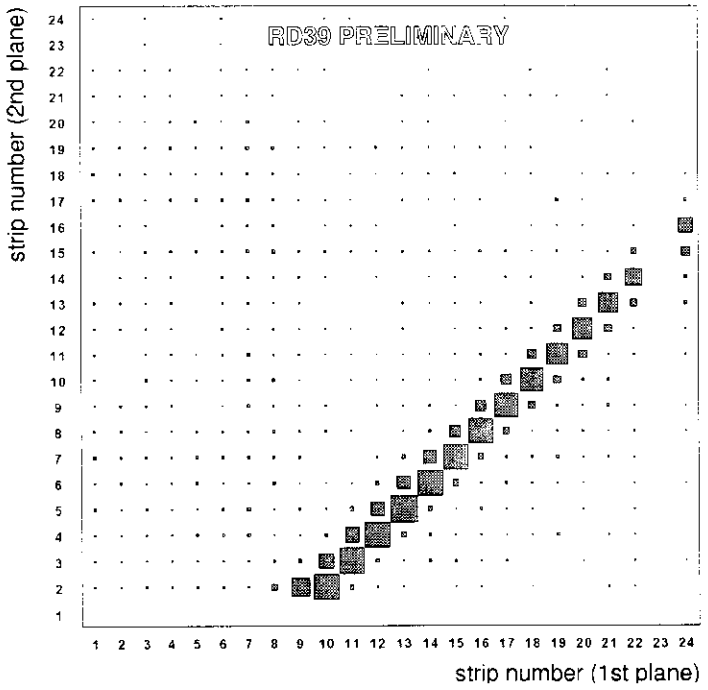


*Figure 28: Asymmetrical correlation between strip numbers on two planes.*

During this test beam period, the detectors received a total dose of about 1 Grad and showed no sign of deterioration of the signal. Having still possibility to increase the bias voltage by

factor of 10 and being able to read signal 10 times smaller, one can be optimistic that the system will be operational up to 100 Grad in the real experiment.

## 5 COOLING SYSTEMS

Two cooling systems using liquid nitrogen ($LN_2$) coolant were designed and built. A simple low-cost static-bath cryostat was optimized for laboratory measurements, while a continuous-flow cryostat was designed for operation in test beams. Work on closed-cycle cooling systems was started; these can use different coolants that cover more narrow temperature ranges and they will enable operation over extended periods in extremely high radiation environment.

### 5.1 Simple static-bath cryostat

A simple $LN_2$ cryostat devoted to CCE measurements was designed and several units were built for laboratory tests at CERN and other institutes of RD39. The cryostat, shown in Fig. 29a, consists of an outer vacuum chamber of 100 mm diameter and an inner $LN_2$ reservoir.

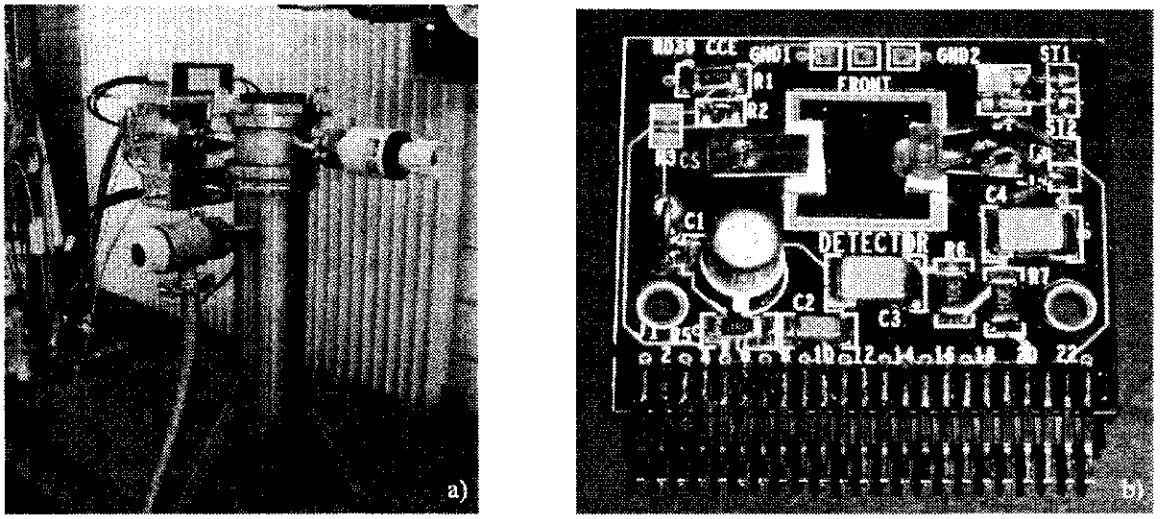


*Figure 29: a) The simple static-bath cryostat; b) The special PCB chip carrier developed for the static-bath cryostat. The heater is located on the back.*

The top flange is equipped with access ports to the vacuum space where the sensor samples are mounted on PCB chip carriers. These ports carry the hermetic-seal feedthroughs for the detector and instrumentation wires, a vacuum gauge, and the vacuum pump-out valve. To reduce thermal radiation heat leak to the PCBs, a radiation shield was attached to the bottom of the inner vacuum chamber of the cryostat. This thin-wall copper shield surrounds the PCBs and the source. Small interchangeable PCB chip carriers, shown in Figure 29b, are mounted

on a larger PCB motherboard which is connected to the $LN_2$ reservoir via a thermal bridge dimensioned so that the temperature of the detectors can be controlled in a reasonable range. The input FET of the preamplifier is located on the chip carrier.

A temperature of 78 K was reached on the detector mount with no applied heat load. A 100 Ω heater was positioned between the chip carriers of the detector under study and of the trigger detector. The heater was soldered on the back of the chip carrier, while the thermometer was fixed on the opposite side. With this setup, it was possible to measure the temperature of the detector accurately and to prevent parasitic noise pickup from the heater by the cold FET. Using a Digital Temperature Controller (model 9650, Scientific Instruments) the sample temperature could be stabilized between 78 K and 250 K.

### 5.2 Continuous-flow cryostat

A continuous-flow $LN_2$ cooling system was designed and constructed by CERN and Karlsruhe University. This allows operating detector modules in a range of temperatures between 80 K and 130 K. The system consists of a top flange equipped with 5 access ports for 5 modules, ports for a $LN_2$ transfer line and a cryogenic needle valve, and additional ports for instrumentation connections. This flange can be optionally connected to a vacuum chamber or a foam-isolated chamber filled by $N_2$ gas. The flange, mounted in vertical position on the vacuum chamber, can be seen in Figure 24.

In the foam-isolated chamber, operation at 80 K is possible by two-phase flow of nitrogen through capillary pipes integrated in the modules, while higher temperature operation requires the flow of gas only in the modules. The cryogenic needle valve allows to control the flow of nitrogen from the transfer line into an open reservoir on the bottom of the foam-isolated chamber. Depending on this flow rate, the reservoir can be filled with liquid or with gas only. In the case that the reservoir is operated with liquid, the nitrogen flowing into the modules becomes subcooled because the capillary pipes connecting the transfer line to the modules are then submerged in $LN_2$ boiling at a saturation pressure which is lower than the pressure in the capillaries.

Operation at higher module temperatures requires the flow of nitrogen gas only in the modules. In this case the cryogenic needle valve is almost closed so that a permanent flow of dry cold nitrogen gas at a slight overpressure prevents back-diffusion of humid ambient air into the foam-isolated chamber.

In the vacuum chamber the cryogenic needle valve can, in principle, be used for controlling the coolant flow through a thermal radiation shield, but it was found that this was not

necessary when some super-isolation was applied around the modules. The control of the module temperature up to 185 K was possible by adjusting the flow through the modules and the power applied by heaters on the modules.

The foam-isolated box has the inner dimensions of 94 x 140 x 370 $mm^3$ and a cold volume of about 4000 $cm^3$. The box is made of rigid 30 mm thick polyurethane foam Alporit which has the effective thermal conductivity of 0.024 W/(K·m) at ambient temperature. The Alporit sheets are covered on each side by a 50 μm thick sheet of aluminum which prevents the diffusion of water into the foam. The density of the foam is 30 $kg/m^3$. Using the conductivity at RT the heat loss from 300 to 80 K through the foam isolation is about 27 W which would give a boil-off rate of 4.9 mMol/s $LN_2$. This estimate is an upper limit, and in practice a much lower flow was used because the sensors could be adequately cooled with the ambient gas at a much higher temperature.

The top flange is made of stainless steel and is 7.5 mm thick. This is clearly not a low-mass component, but was necessary in order to allow a simple stable structure for the vacuum chamber. The flange for the foam-isolated box could easily be made with a lightweight structure, but this was not deemed necessary because in our demonstration runs the particle trajectories did not pass through the flange. The three auxiliary exits of the flange were used to measure the level of the liquid nitrogen and pressure inside the box and the gas flow exhaust from it.

The vacuum-isolated low-loss transfer line from Oxford Instruments has a shutoff needle valve and gas-cooled thermal shield. As was described above, the transfer-line port is connected to a cryogenic needle valve and allows the liquid nitrogen to pass from the transport Dewar vessel to a small copper reservoir inside the Alporit box. The Dewar vessel has an automatic control of the pressure. The cooling of the transfer line takes about 10 minutes and a flow rate of 25 Nl/h is necessary to keep it cold.

The detector modules, shown in Figure 22, were assembled at CERN by gluing glass-epoxy printed circuit boards (PCB) through slots machined on stainless steel flanges (of 65mm diameter and 5mm thickness) with a filled epoxy (Stycast 2850 FT). The glue is resistant to thermal shocks at low temperatures and has a high thermal conductivity. The PCB has 6 copper layers which were designed so that the thermal conduction between the flange and the sensors was low, whereas the transverse conduction was improved by the patterning of the ground layers. A thin-wall capillary pipe of 1.2 mm outer diameter, made of cupronickel (70% Cu, 30% Ni), is soldered along the PCB (Fig. 22). The pipe is fed from the transfer line and its outlet is connected to a flow meter (100Nl/h) and a manual control valve. By

controlling the nitrogen flow rate in the pipe, it is possible to adjust the temperature of the detector. The estimated conduction heat loss along the PCB is less than 2 W. This heat load is absorbed by the cold boil-off gas of the coolant flowing through the pipe soldered onto the neck of the PCB. The minimum flow required to cool the detector area to 83 K at no external heat load was about 10 Nl/h.

The nitrogen flow rate through the pipe on the PCB depends on the pressure of the liquid coming from the transfer line (around 2 bar) and on the control valve setting. If the flow rate is 0.715 mM/s (= 62 Nl/h) which sufficient for absorbing a 4 W heat load at 80 K, the calculated two-phase pressure drop is less than $6 \cdot 10^{-4}$ mbar/cm in the pipe of 1.0 mm inner diameter. One pipe could therefore be used for the cooling of several 4 W modules in series. However, in our present design this is not possible because all modules are supported from RT and therefore require the flow of cold gas in parallel for absorbing the conduction losses along the PCBs.

Figure 30 shows the time evolution of the temperature measured close to the detector on the PCB, at different settings of the nitrogen flow rate through the module. The letters labeling the temperature steps in the graph refer to the table showing the flow rates and the corresponding stable temperatures. All flows are adjusted using manual flow controllers. A LabVIEW program controls the temperature and liquid nitrogen level measurements.

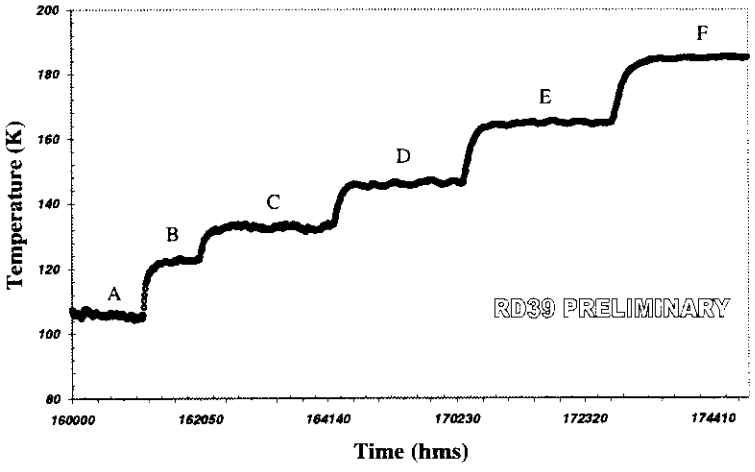


| T(K) | module gas flow rate (l/h) | |
|---|---|---|
| 185 | 50 | F |
| 166 | 60 | E |
| 146 | 70 | D |
| 135 | 80 | C |
| 124 | 90 | B |
| 104 | 100 | A |

*Figure 30: Time evolution of temperature in the continuous-flow cryostat with 1 W power applied simulating two Viking front-end readout chips. The steps of temperature are due to stepwise adjustment of the nitrogen flow rate through the module.*

### 5.3 Closed-cycle refrigerators

Long-term operation requires the use of closed-cycle refrigeration systems in an environment with high radiation field and limited access. The main reasons for this are the safety risks of liquid nitrogen which may become explosive at fluences already below $10^{17}$ p/cm$^2$, and the limited access which precludes the use of transport dewars and forces to use long high-loss transfer lines between the cryostat and the storage tanks located in a more accessible area.

Closed-cycle refrigerators have the advantage that the coolant can be chosen so that operation in the desired temperature range can be controlled by the saturation pressure. The closed-cycle systems based on a single stage, however, are difficult to produce even at 130 K, and therefore we have oriented our studies to multistage systems consisting of an efficient and compact cryogenerator and closed-cycle coolant distribution circuit.

Among the candidate cryogenerators in the 80 – 130 K range are

1) Gifford-McMahon (G-M) cryocoolers

2) Stirling cycle engines

3) Pulse tube refrigerators

4) Cascade Joule-Thomson (J-T) cycle refrigerators

5) Pulse tube refrigerators.

Among these the Stirling cycle engines are presently the most efficient.

The two-phase coolant distribution can be achieved by a condenser and cold liquid recirculator, or by a J-T cycle involving a warm compressor which can be located outside the radiation environment. In some simple systems a heat-tube system could be envisaged, but this will require the cryogenerator at a rather close proximity of the detectors.

The design of the cooling systems will require the knowledge of the heat load from the detectors and front-end electronics. Because the cryogenic silicon sensors draw virtually no current, their main heat load comes from thermal and other radiation, and possibly by conduction through structural elements. Therefore the main heat load is due to the electronics which is currently about 4 mW/channel in circuits such as the ABCD chip of ATLAS SCT operating at 40 MHz clock frequency close to room temperature. One small 40 W Stirling engine combined with a J-T cycle could therefore cool about $10^4$ channels of readout, typical of a sizable beam tracker. A commercial machine with this cooling power uses less than 400 W electrical power [18].

The suitable coolants around 130 K temperature are perfluoromethane $CF_4$, krypton, methane $CH_4$, and argon. Their practical two-phase J-T cycle temperature ranges are between their normal boiling points and critical points listed in Table 1. Nitrogen covers temperatures below this range but is impractical close to its critical point of 125.98 K. It should be noted that the same circuit design and compressor can be used with all of these fluids, and therefore the temperature of operation can be changed simply by evacuating and refilling the two-phase coolant distribution system. The cryogenerators use helium as working fluid.

| Coolant | Normal boiling point | Critical point |
|---|---|---|
| | (K) | (K) |
| $CF_4$ | 145.10 | 227.51 |
| Kr | 119.75 | 209.39 |
| $CH_4$ | 111.67 | 190.60 |
| Ar | 87.27 | 150.65 |

*Table 1: Normal boiling points and critical points of some coolants in the temperature range around 130 K.*

## 6 CONCLUSIONS AND IMPLICATIONS FOR THE LHC EXPERIMENTS

The results presented in this report demonstrate that silicon detectors, irradiated to high doses, recover most of their operating performance when cooled to cryogenic temperatures. Moreover, operation at cryogenic temperatures eliminates the leakage current and permits reliable forward bias operation. The Lazarus effect thus leads to unprecedented radiation hardness for standard silicon detectors. The experimental results reached so far can be summarized as follows.

The CCE of heavily irradiated silicon diodes is recovered at temperatures below 130 K. This temperature corresponds to the maximum achievable CCE for all the detectors studied, and is independent of the irradiation fluence, of the detector structure, and of the polarity of the bias voltage. At temperatures below 130 K, the CCE saturates in the case of forward bias operation, while it slightly decreases under reverse bias.

In the case of reverse bias operation at 77 K, the CCE shows a time evolution after HV turn-on, decreasing from a high value to a reduced saturated value. The time constant depends on the fluence and on the bias voltage, and it is of the order of 3 to 6 minutes. For the most

irradiated sample ($2 \cdot 10^{15}$ n/cm$^2$, 300 μm thick), the saturated value at 250 V and 130 K corresponds to a most probable signal of about 5000 electrons from a MIP.

Detectors irradiated to a fluence of $5 \cdot 10^{14}$ n/cm$^2$ or higher show a negligible bias current for both polarities of the applied bias voltage when operated at cryogenic temperatures. This allows operation under forward bias voltage. In this case, the CCE show no time dependence for all samples. In fact, the measured CCE values do not differ from those observed in reverse bias mode just after turning the HV on. Similar results can also be obtained by increasing the steady-state current in reverse bias by illumination with short wavelength light. In the case of the sample irradiated with $2 \cdot 10^{15}$ n/cm$^2$ (300 μm thick), a most probable signal of about 15'000 electrons can be collected using non-conventional operation.

The "double-p" detector structure is a promising candidate for applications requiring extreme radiation hardness. The sample irradiated with $10^{15}$ n/cm$^2$ yielded a CCE of 84 % at 500 V and 130 K.

In the case of operation at cryogenic temperatures, no effect of reverse annealing process was observed.

Irradiation at a constant temperature of 83 K does not lead to significant deviations from what observed in the case of samples irradiated at room temperature.

In the case of segmented detectors the CCE recovery restores the nominal tracking position resolution. From the analysis of the cluster size and its time evolution, shown in Fig. 19, we can conclude that for the fluence corresponding $1.9 \cdot 10^{14}$ n/cm$^2$ the loss in CCE and its time evolution is mainly due to incomplete depletion.

Having a model of the charge distribution in presence of partial depletion allows a risk assessment in the choice of the detector types in the radiation environment of LHC, assuming that CCE losses are dominated by incomplete depletion. Fig. 31 shows an example of the application of the model for two cases. In Fig. 31a we show the result of modeling a detector which is 300 μm thick, with an 80 μm strip pitch and a binary read-out with a threshold of 6000 ENC and a noise per channel of 1500 ENC, i.e. an ATLAS type detector. It can be clearly seen that in the case of a p-on-n detector, the efficiency for finding a cluster above threshold degrades quickly if only 80% of the depletion voltage can be achieved, while for a n-on-n design even at 50% of the depletion voltage the efficiency is quite acceptable. Another example is shown in Fig. 31b where a 150 μm thick detector with 25 μm strip pitch has been simulated with a threshold of 3000 ENC and a noise per channel of 1000 ENC. This is one of the options of the LHCb vertex detector. Here the efficiency for the p-on-n design would

drop already for a 10% under-depletion, mainly due to the spreading of the cluster over many channels as a result of the small pitch compared to the thickness of the non-depleted layer. On top of that the resolution is expected to degrade quickly.

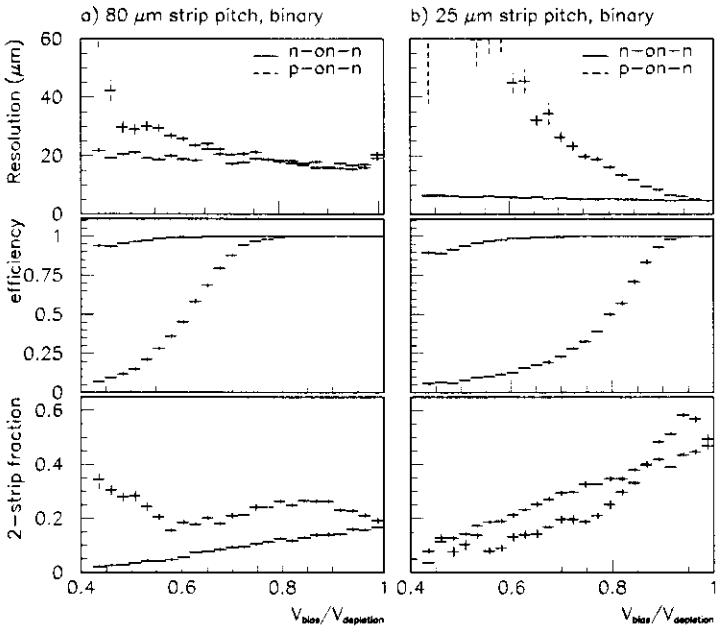


*Figure 31: Expected performance for two different detector types with binary readout as a function of $V_{bias}/V_{depletion}$ (assuming no trapping effects). (a) Shows a 300 μm thick detector with 80 μm strip pitch. A threshold of 6000 ENC for a noise of 1500 ENC per channel is assumed. (b) Shows a 150 μm thick detector, 25 μm strip pitch and a threshold of 3000 ENC for a noise per channel of 1000 ENC.*

Our tests of the continuous-flow $LN_2$ cooling system indicate that detectors can be operated both in vacuum and in foam-isolated chambers filled with dry nitrogen at ambient pressure. The design of detector modules is greatly simplified by the fact that the sensor self-heating is negligible. Moreover, the annealing studies indicate that the sensors can be warmed up during shutdown and maintenance periods without significant effect on performance.

In the LHC experiments the preferred cooling method is based on compact closed-cycle systems which we are presently investigating.

The fast detector backplane signals can be used for triggering purposes. With MIP signals this may require a fast low-noise preamplifier mounted on the detector module, whereas with heavy ions the signal is large enough so that the amplifier can be located outside the cryostat if a high-quality coaxial line is used.

Our preliminary tests indicate that the detector edge surface current is negligible at cryogenic temperatures. This can lead to the possibility of designing edge-sensitive structures in which the sensitive volume extends very close to the side of the sensor. These may enable to bring the tracking devices closer to the beam in the Roman pot detectors of LHC experiments.

## 7 FUTURE PROGRAMME

In our Addendum of 1998 we noted that our limited resources were not sufficient for the development and optimization of cryogenic readout electronics, and we therefore proposed to focus on the sensor development. Because these studies have now been successfully accomplished, as shown by our published and preliminary results, we are now proposing to move to developing, designing and testing realistic detector modules which require adequate front-end electronics. Knowing from our preliminary tests that the deep sub-micron radiation-tolerant circuits [19] work well at low temperatures, similar to the usual CMOS circuits which we have already used, we propose to investigate and use the APV25 microstrip readout chip in the first electrical modules to be assembled. Later we could also consider the Alice pixel readout chip when it becomes available.

Our planned work program, approved unanimously in our collaboration meeting of 2-3 December 1999, includes the following:

1) Studies of detector module materials which are compatible with cryogenic operation;

2) Development of precision micro-assembly methods for cryogenic modules, and the assembly of prototype modules;

3) Studies of the deep-submicron radiation-tolerant circuits over extended temperature range;

4) Design of cryogenic silicon microstrip or pixel sensors suitable for Roman pot detectors, in collaboration with the LHC experiments, with a particular focus on edge-sensitive sensors;

5) Design and construction of cryogenic Roman pots and prototype detector modules in collaboration with the LHC experiments;

6) Design and construction of a prototype closed-cycle cooling system for Roman pot detectors.

We also plan to apply this technology to devices for monitoring the luminosity in the high-flux regions of the LHC experiments, and for use in LHC magnet cryostats, both for luminosity monitoring and for beam loss monitoring.

We have already discussed our plans and program with several LHC experiments and the LHC Beam Instrumentation group, and it appears clear to all parties that a common program with shared resources would be profitable.

The estimated duration of our proposed project is two years and would require additional dedicated manpower. This can only partly be drawn from the approved experiments and we are therefore asking for additional fellows and/or doctoral students dedicated to the RD39 program.

We further request 20 $m^2$ additional space in the CERN Cryolab and their technical support at the present level, and the technical support of the CERN Microelectronics group for the readout circuitry and assembly of the modules.

We estimate that our program would require 6 weeks of test beam time, in short periods, during the two year project.

It is expected that the funding of our program will be covered by the collaborating institutes, including CERN.

## 8 ACKNOWLEDGEMENTS

This work would not have been possible without the enthusiastic support of several CERN experiments, including in particular the NA50, COMPASS and LHCb, and we are grateful to their management and participating members. The contributions and support of the CMS, TOTEM and ATLAS experiments are also greatly appreciated and acknowledged. We have furthermore profited from discussions with the Beam Instrumentation group and would like to thank them for their advice and support.

References


[1] RD39 Collaboration, K. Borer et al., CERN/LHCC 98-27, DRDC P53 Add. 1, 12 August 1998.

[2] V. Palmieri et al., Nucl. Instr. and Meth. in Phys. Res. **A413** (1998) 475.

[3] K. Borer et al. (RD39 Collaboration), "*Charge collection efficiency of irradiated silicon detectors operated at cryogenic temperatures*", preprint CERN-EP/99-102, Nucl. Instr. and Meth. in Phys. Res. **A**, in press.

[4] K. Borer et al., "*Charge collection efficiency and resolution of an irradiated double sided silicon microstrip detector operated at cryogenic temperatures*", preprint CERN-EP/99-98, Nucl. Instr. and Meth. in Phys. Res. **A**, in press.

[5] V. Chabaud et al., Nucl. Instr. and Meth. in Phys. Res. **A368** (1996) 314.

[6] E.S. Kristof, "*Characterisation of Neutron Flux in the Exposure Channel F19 of the TRIGA Mark II Reactor in Ljubljana*", Proceedings of Nuclear Energy in Central Europe '98, Terme Catez, Slovenia, September 7-10, 1998, p. 43.

[7] A.M. Ougouag et al., IEEE Trans. Nucl. Sci., **NS-37** (1990) 2219.

[8] P.J. Griffin et al., preprint SAND92-0094, Sandia Natl. Lab., 1993.

[9] RD48 Collaboration, V. Augelli et al., CERN/LHCC 98-39, LEB Status Report/RD48 21 October 1998.

[10] V. Eremin et al., Sov. Phys. & Techn. of Semiconductors **8** (1974) 1157.

[11] B. Dezillie, V. Eremin and Z. Li, IEEE Trans. Nucl. Sci., NSS/MIC98 Conference Issue, **46** (1998) 221.

[12] L.J. Beattie et al., in Proc. Elmau Workshop "*New Developments on Radiation Detectors*", 8th European Symposium on Semiconductor Detectors, Schloß Elmau, June 14-17, 1998 (to be published); A. Chilingarov and T. Sloan, Nucl. Instr. and Meth. in Phys. Res. **A399** (1997) 35.

[13] Z. Li and H.W. Kraner, IEEE Trans. Nucl. Sci. **NS-38** (1991) 244.

[14] L. Beattie et al., Nucl. Instr. and Meth. in Phys. Res. **A412** (1998) 238.

[15] B. Dezillie, V. Eremin, Z. Li and E. Verbitskaya, *Polarization of Silicon Detectors by Minimum Ionizing Particles*, submitted to Nucl. Instr. and Meth. in Phys. Res. **A**.

[16] Proceedings of the 3rd European Workshop on Low Temperature Electronics (WOLTE 3), Journal de Physique IV (Proceedings) **8** (1998)

[17] G. Cicalo et. al., "*Study of Dimuon and Charm Production with Proton and Heavy Ion Beams at the CERN SPS*", Letter of Intent CERN / SPSC 99-15, SPSC / I221, 7 May 1999

[18] O. Hempel, A. Tscheutschler, A. Binner, R. Herzog and O. Zettl, in Proc. 20$^{th}$ Int. Congress of Refrigeration, IIR/IIF, Sydney 1999 (to be published).

[19] RD49 Collaboration, L. Adams et al., CERN/LHCC 98-8, LEB Status Report/RD49 8 March 1999.